UNIVERSIDAD SANTIAGO DE CHILE

FACULTAD DE CIENCIAS

Departamento de Física

Electron transport in driven nanojunctions

Felipe Alexis Recabal Rivas

Profesor Guía: Felipe Herrera Urbina

Tesis presentada en el cumplimiento de los
requisitos para la obtención del grado de:
Magíster en Ciencias con mención en Física

Santiago de Chile, Chile

2021

Resumen

Nanojunturas ofrecen la posibilidad de estudiar las propiedades de transporte a través de materiales nanométricos, como puntos cuánticos o moléculas individuales, unidos a cables eléctricos. Hoy en día, el progreso de técnicas experimentales y métodos teóricos ha permitido entender interesantes fenómenos de transporte cuántico, con alcances como bloques de construcción de circuitos electrónicos.
En la siguiente Tesis estudiamos el transporte de electrones a través de nanojunturas impulsadas. Desarrollamos un modelo donde la nanojuntura es tratada sistema cuántico abierto, donde el material nanométrico, modelado como un arreglo conductor de sitios de electrones, interactúa con un ambiente compuesto por reservorios de muchos cuerpos. Obtuvimos la dinámica de la nanojuntura como una ecuación maestra cuántica de Lindbland, la cual incorpora las interacciones como transiciones de electrones inducidas entre los autoestados del arreglo conductor. Resolviendo numéricamente la dinámica de la nanojunctura en el régimen estacionario, caracterizamos la nanojuntura basados en observables como la corriente eléctrica a través de la nanojuntura mientras un voltaje de polarización es aplicado.
Nuestros resultados muestran que dinámica puramente de tuneleo explica régimen estacionario a escalas de tiempo relacionados con el inverso de las tasas de tuneleo, picos de conductancia a voltajes donde la condición resonante es satisfecha, y, cuando es incorporado el efecto de un voltaje de puerta, la disminución de la conductancia a medida que la temperatura disminuye, pero el efecto Kondo no es apropiadamente descrito en nuestra ecuación maestra cuántica de Lindbland. Procesos como emisión espontánea y relajación por fonones, explica el comportamiento de las poblaciones para un conjunto de autoestados afectados por ellos, produciendo que sus contribuciones a la corriente a la interfase izquierda y derecha sean diferentes. El transporte de electrones es dependiente the la geometría del arreglo conductor, pero alcanzando un valor similar de corriente de saturación, ya que procesos que limitan el transporte como la interferencia cuántica no son apropiadamente descritos en nuestra ecuación maestra cuántica de Lindbland. Cuando es aplicada una fuente de bombeo incoherente al arreglo conductor, nuestros resultados muestran los efectos de luz inducida por corriente y corriente inducida por luz, permitiendo inclusive una corriente fotoeléctrica a configuraciones donde el voltaje de polarización es cero cuando las tasas de tuneleo a la izquierda y derecha son diferentes, mientras que dirección de la corriente fotoeléctrica inducida depende de si el arreglo conductor tiene electrones deslocalizados en el conjunto de orbitales base o excitados.

Palabras claves: Junturas moleculares, puntos cuánticos, sistemas cuánticos abiertos, transport de electrones, ecuación maestra cuántica.

Abstract

Nanojunctions offer the possibility to studying the transport properties through driven nano-sized materials, as quantum dots or single molecules, attached to electric leads. To the day, the progress of experimental techniques and theoretical methods has allowed to understand interesting quantum transport phenomena, with scopes as building block of electronic circuits.

In the following Thesis we study the electron transport through nanojunctions. We developed a model where the nanojunction is treated a open-quantum system, where the nano-sized material, modelled as a conducting array of electron sites, interact with a environment composed by many-body reservoirs. We obtain the nanojunction dynamics as a Lindbland quantum master equation, which incorporates the interactions as induced electron transitions between the conducting array eigenstates. Solving numerically the nanojunction dynamics at the stationary regimen, we characterize the nanojuction based on observables as the electric current through the nanojunction while a bias voltage is applied.

Our results show that pure tunneling dynamics explain stationary regimen at time scale related with the inverse of tunneling rates, conductance peak at voltage where the resonant condition is satisfied, and, when is incorporated the effect of gate voltage, the decreasing of conductance at time that temperature decreases, but Kondo effect is not appropriately described in our Lindbland quantum master equation. Processes as spontaneous emission or phonon relaxation, explain the behaviour of populations on a set of eigenstates affected by them, producing that their contribution to the current at the left-right interfases are different. Electron transport is dependent of conducting array geometries, but reaching similar saturated current value, because processes which limits the transport as quantum interference are not appropriately described in our Lindbland quantum master equation. When is applied an incoherent pumping source to the conducting array, our results show the effects of current-induced light and light-induced current, allowing even a photocurrent at zero bias configuration when the left-right tunneling rates are different, while the induced photocurrent direction depends on whether the conducting array has delocalized electrons in the ground or the excited orbital manifold.

Key words: Molecular junctions, quantum dots, open-quantum systems, electron transport, quantum master equation.

Acknowledgement

This work was funded by the National Agency for Research and Development (ANID) through Becas de Magíster Nacional 2020 - 22200493, and Iniciativa Científica Milenio (ICM) through the Millennium Institute for Research in Optics (MIRO).

Contents

1 Introduction **1**

1.1 Quantum dots . . . 1

1.2 Molecular junctions . . . 3

1.3 Some quantum transport phenomena . . . 4

2 Nanojunction description **6**

2.1 Density operator formalism . . . 6

2.1.1 Quantum-mechanical systems . . . 6

2.1.2 Populations and coherences . . . 8

2.1.3 Reduced density operators . . . 8

2.1.4 Thermal-equilibrium density operators . . . 9

2.2 Model of nanojuction . . . 10

2.2.1 Second quantization theory . . . 10

2.2.2 Conducting array . . . 12

2.2.3 Environment . . . 14

2.2.4 Interactions . . . 16

3 Nanojunction dynamics **19**

3.1 Quantum master equation . . . 19

3.1.1 Rate equations . . . 22

3.2 Nanojuction characterization . . . 23

3.2.1 Current-voltage . . . 23

3.2.2 Gate voltage . . . 24

4 Results **25**

4.1 Electron transition processes . . . 26

4.1.1 Resonant tunneling . . . 26

4.1.2 Spontaneous emission . . . 31

4.1.3 Phonon relaxation . . . 33

4.2 Geometric array dependence . . . 35

4.3 Incoherent pumping . . . 37

Conclusions **41**

Bibliography 43

Appendix 47

A Redfield equation 48

B Lindbland quantum master equation 50

C Reservoir particles evolution 54

List of Tables

4.1 Model parameters 26
4.2 Eigenstates for a single-level conducting array with spin. 30
4.3 Eigenstates for a two-level conducting array. 31
4.4 Eigenstates for a two-site conducting array 33

B.1 System and reservoir part of interaction Hamiltonians. 51
B.2 Effective transfer rates. 53

List of Figures

1.1 Vertical and lateral quantum dot structures. 2
1.2 Some reported quantum electron transport processes in nanojunctions. 3
1.3 Techniques for implementation of molecular junctions. 5

2.1 Scheme of macroscopic metals and molecular junction. 7
2.2 Model of nanojunction. 10

3.1 Scheme of open-quantum system treatment and the dynamics induced in the quantum system. 20
3.2 Conducting array dynamics induced by the electron tunnelling with the leads. 23

4.1 Nanojunction for one level conducting array and time-dependent dynamics induced by resonant tunnelling. 27
4.2 Electron transport in nanojunction for one level conducting array. 28
4.3 Electron transport in nanojunction for one degenerated spin level conducting array. . 29
4.4 Nanojunction and electron transport in two level conducting array. 31
4.5 Microscopic effect of spontaneous emission. 32
4.6 Nanojunction and electron transport in two level conducting array. 33
4.7 Microscopic effect of phonon relaxation. 34
4.8 Nanojunction and electron transport in geometric conducting arrays 35
4.9 Microscopic effect on nanojunction in geometric conducting arrays. 36
4.10 Electron transport in nanojunction in circular symmetrical and non-symmetrical conducting arrays. 36
4.11 Nanojunction and electron transport affected by incoherent pumping in excited hopping conducting arrays. 38
4.12 Microscopic effect of incoherent pumping in excited hopping conducting arrays at zero bias. 39
4.13 Nanojunction and electron transport affected by incoherent pumping in ground hopping conducting arrays. 40

Chapter 1

Introduction

Based on the progress of different experimental techniques and theoretical methods, nano-sized materials attached to leads, i.e. nanojuctions, have received substantial interest in the last decades as a route for studying non-equilibrium many-body quantum physics at the nanoscale [Thoss and Evers, 2018]. Experiments has shown that many of these nano-sized materials behaves as a "quantum dots", where the electrons are confinement in the space and described by discrete quantum states [Andergassen et al., 2010]. The quantum description of nanojunctions explains the plethora of interesting transport phenomena, which could be the basis of future applications because the promised reduction of energy consumption, increasing capability and cheaper manufacturability of electronic circuits [Sowa et al., 2017].
In the following Chapter is given a brief introduction to nanojunctions, focusing in quantum dots and molecular junctions devices, which are some of the most studied systems. Are also explained some interesting transport phenomena, giving some basic definitions.

1.1 Quantum dots

Quantum dots are low-dimensional system where are trapped few conduction electrons. The name refers to devices where electrons are confinement in the three spatial dimension. The typical size of quantum dot oscillates between few to hundred of nanometers, which contains from 10^3 to 10^6 atoms with equivalent number of electrons, but the confinement produces that only few electrons are free, while the other are bounded to the atomic nucleus [Tartakovskii, 2012, Kouwenhoven et al., 1997]. Because the small size of quantum dots, this free electrons are distributed in discrete quantum states and having a charging energy for add a new electron, analogous to the ionization potential[1] in atoms. Therefore quantum dots has been considerer as "artificial atoms", while multiple coupled quantum dots has been consider as "artificial molecules" [Kouwenhoven, 1995].

[1] The spending energy for removing an electron from an atom.

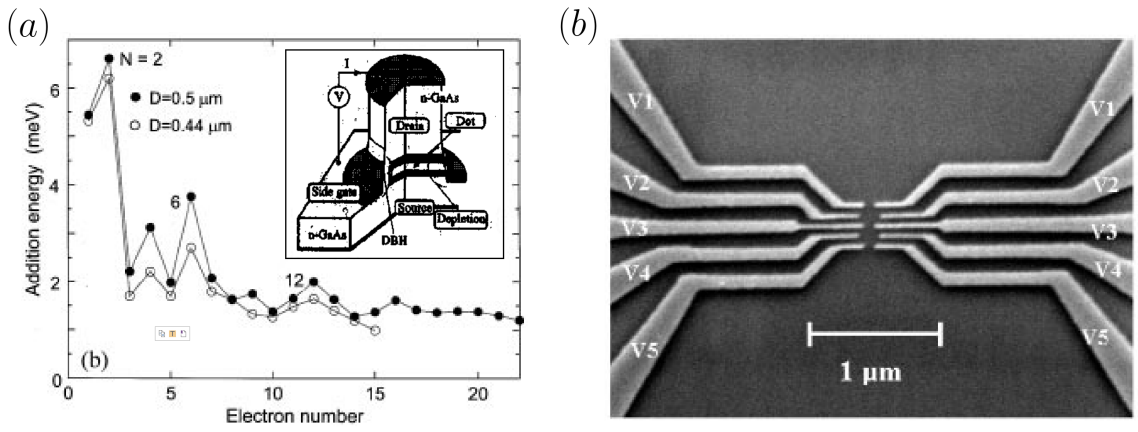

Figure 1.1: (a) Addition energy in function of electron number N of vertical quantum dot whit diameters D (inset: vertical quantum dot structure composed semiconductor materials, where could be applied a voltage V and a gate voltage); (b) coupled quantum dot in a lateral structure, where ten independently tunable gates squeeze the electron gas of the GaAs/AlGaA heterostructure. Panels (a) and (b) adapted from [Tarucha et al., 1996] and [Jeong et al., 2001], respectively.

As artificial atoms, for vertical quantum dots, an structure formed by etched pillars of semiconductor materials where the quasi-two-dimensional island of electron is squeezed by gate voltage applied through the metallic side around the vertical structure (see inset in Fig. 1.1(a)), the results of current in function of gate voltage for small bias voltage has shown that addition energy for charging the quantum dot from N to $N+1$ electrons is according to the filling of an 2D harmonic potential, where the big peaks at $N = 2, 6$ and 12 represent the close shell structure, while the filling of the middle region is consequence of alignment Hund's rules, as is shown in Fig. 1.1(a), analogous to atomic ionization spectra [Tarucha et al., 1996, Reimann and Manninen, 2002].
For studying electron transport, an other common way to fabricated quantum dot or coupled quantum dots is depositing gates over a two-dimensional electron gas formed by a mesoscopic semiconductor heterostructure (typically GaAs/AlGaAs), where the electrostatic effect of an applied voltage by the gates tend to electrostatically creates a bowl-like potential, which confines the electron in the lateral direction [Reimann and Manninen, 2002], as in shown in Fig. 1.1(b). Therefore, the quantum dot is limited to an small region of a semiconductor material of typical size of 100 nanometers [Kouwenhoven et al., 1997].

Quantum dots are used for studying many-body properties of a finite fermionic systems with scope on areas such as chemistry, medicine and material science, based in the possibility of register current and voltage leads while is changed the electrostatic gates, dot geometry or magnetic field, unlike of real atoms [Tartakovskii, 2012, Reimann and Manninen, 2002].

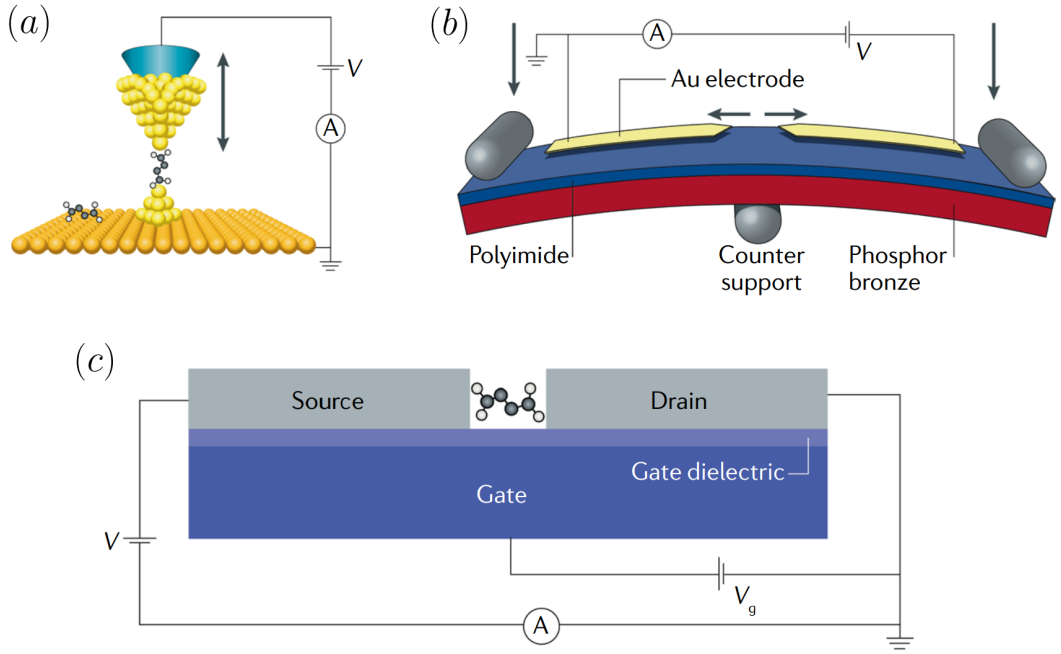

Figure 1.2: Techniques of molecular junction fabrication, where a bias voltage (V) is applied while is measured a current (A); (a) Scanning tunneling microscope break junction; (b) Mechanically controllable break junctions; and (c) Electromigration break junctions, which offer the posibility of adding a gate voltage (V_g). Adapted from [Gehring et al., 2019].

1.2 Molecular junctions

Molecular junctions refers to system where a single molecule, as small as one nanometer, is placed between two metallic or semiconductor leads, measuring its transport properties [Evers et al., 2020]. Its development has been framed in a field called *molecular electronic*, which study electronic and thermal transport in circuit composed by individual molecules, and has allowed to answer basic questions and quantum phenomena [Scheer and Cuevas, 2017, Thoss and Evers, 2018].

Transport of single molecules was theoretically first proposed by Aviram and Ratner at 1974 [Aviram and Ratner, 1974], but it was not until 1997, based in techniques for the development of metallic wires at the end of the 1980's and the beginning of the 1990's, that was shown in [Reed et al., 1997, Scheer and Cuevas, 2017] the first experiment of single molecules, showing the rectifier behaviour theoretically predicted. At the date, the most frequent techniques to implement molecular junctions are [Gehring et al., 2019, Evers et al., 2020]:

- Scanning tunneling microscope break junction: The tip of an STM is pushed repeatedly on the metallic substrate, where molecules are deposited, and retracted, as is shown in Fig. 1.2(a). The gap formed between the tip and the substrate is small enough to bridge molecules, which are measured as the conductance in function of distance while a bias voltage is applied.

- Mechanically controllable break junctions: A notched or lithographically fabricated metallic wire is deposited on the top of a flexible substrate. The system is bending, using a three point mechanism, until the wire breaks, as is shown in Fig. 1.2(b). The gap in controlled relaxing the bending while evaporated single molecule in the environment could be attached to the leads, measured as a non-zero current.

- Electromigration (EM) break junctions: A metal wire is deposited over a dielectric using lithography techniques, where an applied voltage rampe creates by electromigration[2] a gap small enough to form a bridge for a single molecule, as is shown in Fig. 1.2(c). Molecules could be deposited onto the wire before or after the electromigration. Unlike with the other techniques, EM break junctions offer the posibility of adding a third gate, which add an electrostatic effect by a gate voltage V_g.

1.3 Some quantum transport phenomena

A plethora of interesting quantum transport phenomena has been reported. In the following is explained some of them:

- Coulomb blockade: In a tree gate system, when a gate voltage induces an electrostatic change of the quantum dots or single molecule energies continuously, it could be charged by the electrons tunneled from the leads, measured as a conductance peak at small bias voltage. Coulomb blockade occurs when the addition of a single-electron is avoided if the charging energy is greater than the thermal energy [Reimann and Manninen, 2002, Tartakovskii, 2012]. At the Coulomb blockade regime, the conductance peaks of a single electron tunneling looks as periodic oscillations, known as Coulomb oscillations [Kouwenhoven et al., 1997], as is shown in Fig. 1.3(a).

- Kondo effect: At low temperature is appreciate a doublet of some conductance peak, because the Coulomb interaction of opposite spins in the same state [Yoffe, 2001]. When is measured the conductance in function of the temperature in the middle region, a non-monotonic behaviour of resistance is produced, as is shown in Fig. 1.3(b), first reported by Kondo in metals containing magnetic impurities [Kondo, 1964]. The Kondo effect has been attributed to the strong correlations between spin electrons at low temperature, and has been reported in molecular junctions and quantum dots. For bulk material, the Kondo effect decreases the transport because it increases the electron scattering by the impurities, while in quantum dots or molecular junctions it enhances the transport, because the electron are transport only through these electron sites [Inoshita, 1998].

[2]The electromigration is the process where conducting electron driven a diffusion of atoms under large current.

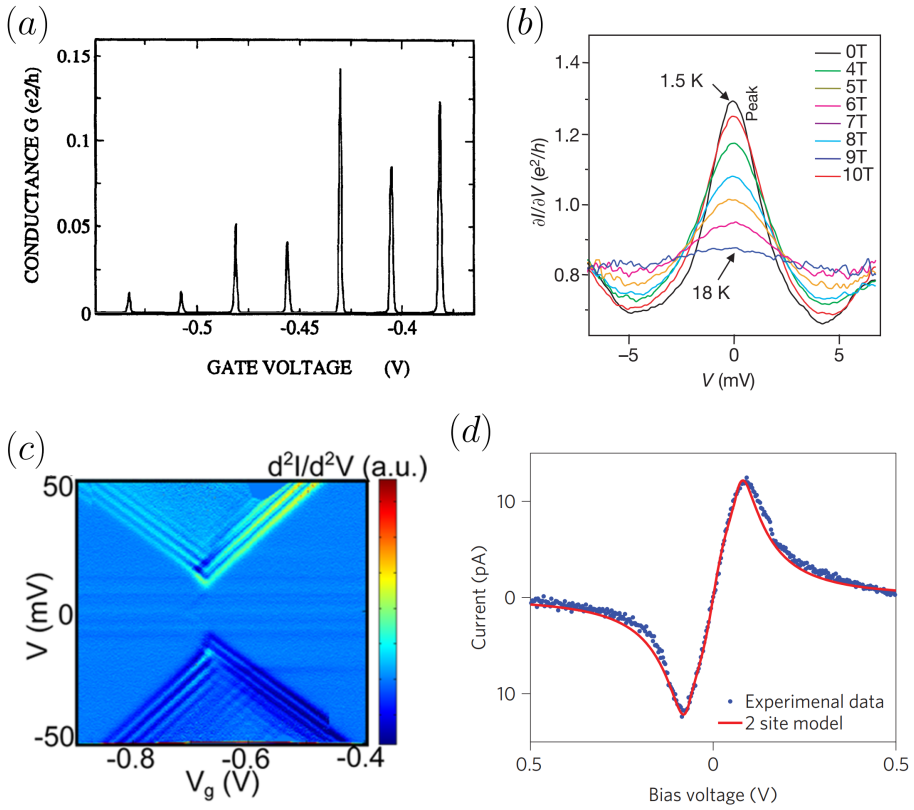

Figure 1.3: Some reported quantum transport phenomena; (a) conductance in function of gate voltage for zero bias voltage for a quantum dot system, which shows Coulomb oscillations; (b) conductance in function of gate voltage for different temperature for a molecular junction system, which shows a Kondo peak; (c) derived conductance in function of gate voltage and bias voltage for a molecular junction system, which shows Franck-Condon blockade; and (d) current-voltage curve for a molecular junction system, which shows negative differential conductance. Panels (a), (b), (c) and (d) adapted from [Kouwenhoven et al., 1991], [Park et al., 2002], [Burzurí et al., 2014] and [Perrin et al., 2014], respectively.

- Franck-Condon blockade: When the electrons are strongly coupled to a vibrational mode, the transport properties are affected, associated to the apparition of transport phenomena. One of them is the Franck-Condon blockade, where the single-electron tunneling is suppressed at low bias for any gate voltage, as is shown in Fig. 1.3(c), and has been reported in molecular junctions [Burzurí et al., 2014] and carbon nanotubes quantum dots [Leturcq et al., 2009].

- Negative differential conductance: Negative differential conductance correspond to an effect where the electron current decreases while a bias voltage is increasing over an specific range, as is shown in Fig. 1.3(d). It was first reported in p-n junctions and semiconductor heterostructure, but also appears in quantum dots and molecular junction systems [Xue et al., 1999]. This has been attributed to narrow feature of the density of states of the tip apex atom in STM [Xue et al., 1999], conformational changes, spin blockade, phonon blockade or suppressed resonant transport [Perrin et al., 2014].

Chapter 2

Nanojunction description

In macroscopic metals, the conductance G follows the Ohm law according to,

$$G = \sigma \frac{S}{L}, \tag{2.1}$$

where σ is its the conductivity, S is the traversal area and L is the length, as is shown in Fig. 2.1(a). Nevertheless, in nanojunctions, because the size of the attached material, for example the single molecule in Fig. 2.1(b), the electron transport happens in the quantum regime, which produces, in general, non-Ohmic behaviour [Scheer and Cuevas, 2017]. It means, this kind of systems need to be described as a quantum system.
In the following Chapter is developed quantum description of nanojunctions, based in density operator approach and second quantization theory. The nanojunction is modelled doing different approximation, capturing or ignoring some electron transference processes.

2.1 Density operator formalism

Despite any quantum-mechanical system could be described through a wave function, in this work the system is described by a density operator, because the system dynamics is reduced to a compact and reduced number of equations for many-particle systems and macroscopic observables [Breuer et al., 2002, Nitzan, 2006].

2.1.1 Quantum-mechanical systems

A quantum-mechanical system is described by a wave function $|\Psi(t)\rangle$, which evolves through the Schrödinger equation ($\hbar = 1$),

$$\frac{d}{dt} |\Psi(t)\rangle = -i\hat{\mathcal{H}} |\Psi(t)\rangle , \tag{2.2}$$

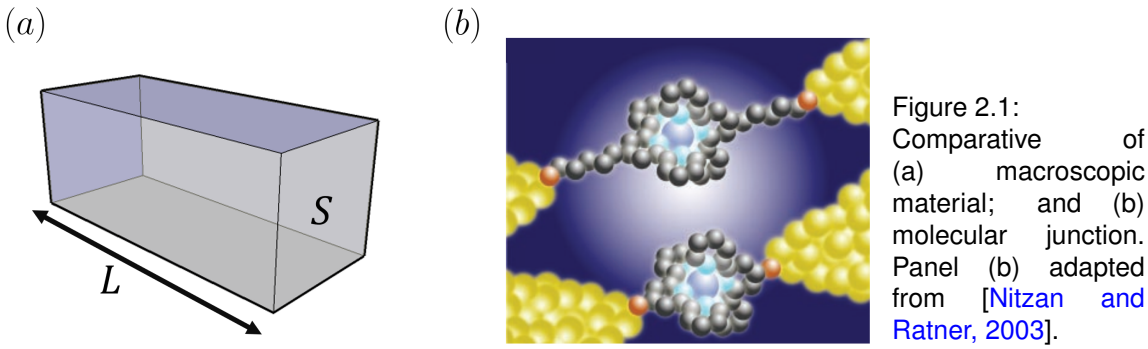

Figure 2.1: Comparative of (a) macroscopic material; and (b) molecular junction. Panel (b) adapted from [Nitzan and Ratner, 2003].

where $i = \sqrt{-1}$ is the imaginary unit and $\hat{\mathcal{H}}$ is the system Hamiltonian. Writing the Hamiltonian $\hat{\mathcal{H}}$ in diagonal form as,

$$\hat{\mathcal{H}} \left|\phi_n\right\rangle = \omega_n \left|\phi_n\right\rangle , \tag{2.3}$$

are defined the system eigenstates (or eigenbasis) $\{|\phi_n\rangle\}$ and the eigenenergies (or spectrum) $\{\omega_n\}$. Because the eigenstates $\{|\phi_n\rangle\}$ defines a basis in the system space, the wave function of the system $|\Psi(t)\rangle$ could be written as,

$$\left|\Psi(t)\right\rangle = \sum_n C_n(t) \left|\phi_n\right\rangle , \qquad C_n(t) = \left\langle\phi_n \middle| \Psi(t)\right\rangle , \tag{2.4}$$

where the time-dependent coefficients, $C_n(t)$, satisfies,

$$\left|\left\langle\Psi(t)\middle|\,\Psi(t)\right\rangle\right|^2 = 1 \longrightarrow \sum_n |C_n(t)|^2 = 1, \tag{2.5}$$

because the normalization of the wave function along the time t.

The average of any physical observable of the system associated to an operator $\hat{\mathcal{A}}$, based in the system wave function in Eq. (2.4), is computed in function of time as,

$$\langle\hat{\mathcal{A}}\rangle = \left\langle\Psi(t)\middle|\,\hat{\mathcal{A}}\,\middle|\Psi(t)\right\rangle = \sum_{n,m} C_n(t) C_m^*(t) \mathcal{A}_{m,n} \equiv \sum_{n,m} \rho_{n,m}(t) \mathcal{A}_{m,n}, \tag{2.6}$$

where $\mathcal{A}_{m,n} = \left\langle\phi_m\middle|\,\hat{\mathcal{A}}\,\middle|\phi_n\right\rangle$ is an element of $\hat{\mathcal{A}}$ and $\rho_{n,m}(t) = \left\langle\phi_n\middle|\,\hat{\rho}(t)\,\middle|\phi_m\right\rangle$ is an element of the system density operator $\hat{\rho}$, defined as,

$$\hat{\rho}(t) = \left|\Psi(t)\right\rangle \left\langle\Psi(t)\right| , \tag{2.7}$$

which stores information about the system. With the density operator in Eq. (2.7), the average of the observable $\hat{\mathcal{A}}$ in Eq. (2.6) is reduced to,

$$\langle\hat{\mathcal{A}}\rangle = \mathrm{Tr}\left[\hat{\rho}(t)\hat{\mathcal{A}}\right] , \tag{2.8}$$

where Tr correspond to a trace over the system space. The results above were derived using the eigenbasis $\{\phi_n\}$, but is valid for any basis in the system space.

Based in the Schrödinger equation in Eq.(2.2) and the density operator in Eq. (2.7), the evolution of the density operator is given by the Liouville's equation,

$$\frac{d}{dt}\hat{\rho}(t) = -i\left[\hat{\mathcal{H}}, \hat{\rho}(t)\right], \tag{2.9}$$

where $\left[\hat{\mathcal{H}}, \hat{\rho}(t)\right] = \hat{\mathcal{H}}\hat{\rho}(t) - \hat{\rho}(t)\hat{\mathcal{H}}$ is the commutator.
Therefore, the density operator and the Liouville's equation are an alternative way for describing quantum-mechanical systems, while the Eq. (2.8) is a way for computing average of observables.

2.1.2 Populations and coherences

For any density operator $\hat{\rho}$, exist a basis $\{|\psi_\alpha\rangle\}$ where it takes a diagonal form, it is,

$$\hat{\rho} = \sum_\alpha \rho_\alpha |\psi_\alpha\rangle \langle\psi_\alpha|, \tag{2.10}$$

where ρ_α correspond to the system probability (or population) at the state $|\psi_\alpha\rangle$. For representing the density operator in other basis, for example the Hamiltonian basis $\{|\phi_n\rangle\}$ (see Eq. (2.3)), is used a change of basis according to,

$$|\psi_\alpha\rangle = \sum_n a_{\alpha,n} |\phi_n\rangle, \qquad a_{\alpha,n} = \langle\phi_n |\psi_\alpha\rangle, \tag{2.11}$$

where $a_{\alpha,n}$ are time-independent coefficients. Applying the change of basis in Eq. (2.11), the density operator in Eq. (2.10) becomes,

$$\hat{\rho} = \sum_{n,m} \rho_{n,m} |\phi_n\rangle \langle\phi_m|, \qquad \rho_{n,m} = \sum_\alpha \rho_\alpha a_{\alpha,n} a^*_{\alpha,m}, \tag{2.12}$$

where the terms $\rho_{n,m}$ are know as coherences when $n \neq m$ or populations when $n = m$.

2.1.3 Reduced density operators

Consider a system composed by two sub-systems $\mathcal{A}$ and $\mathcal{B}$. The general form of writing the system density operator $\hat{\rho}$ in terms of the basis $\{|a\rangle\}$ and $\{|b\rangle\}$ for $\mathcal{A}$ and $\mathcal{B}$ sub-systems, respectively, is according to,

$$\hat{\rho} = \sum_{a,b} \rho_{ab,a'b'} |ab\rangle \langle a'b'|, \tag{2.13}$$

where $\rho_{ab,a'b'} = \langle ab|\,\hat{\rho}\,|a'b'\rangle$ is an element of the density operator and the state $|ab\rangle = |a\rangle \otimes |b\rangle$ is constructed as a tensor product ($\otimes$) between the state $|a\rangle$ and $|b\rangle$. For an observable associated to an operator $\hat{\mathcal{A}}$ in the sub-system $\mathcal{A}$, is computed as (see Eq. (2.8)),

$$\langle\hat{\mathcal{A}}\rangle = \mathrm{Tr}\left[\hat{\rho}\hat{\mathcal{A}}\right] = \sum_{ab}\sum_{a'b'} \rho_{ab,a'b'} \langle a'b'|\,\hat{\mathcal{A}}\,|ab\rangle, \tag{2.14}$$

where Tr is the trace over the sub-systems $\mathcal{A}$ and $\mathcal{B}$. Because $\hat{\mathcal{A}}$ belongs only in the space of the sub-system $\mathcal{A}$, the term $\langle a'b'|\,\hat{\mathcal{A}}\,|ab\rangle$ is reduced to $\langle a'|\,\hat{\mathcal{A}}\,|a\rangle\,\delta_{b,b'}$. Therefore, the observable in Eq.

(2.14) is reduced to,

$$\langle \hat{\mathcal{A}} \rangle = \sum_{ab} \sum_{a'} \rho_{ab,a'b} \langle a' | \hat{\mathcal{A}} | a \rangle \equiv \mathrm{Tr}_{\mathcal{A}} \left[\hat{\rho}_A \hat{\mathcal{A}} \right], \tag{2.15}$$

where $\mathrm{Tr}_{\mathcal{A}}$ is the trace over the sub-system $\mathcal{A}$, and is defined the density operator of the sub-system $\mathcal{A}$,

$$\hat{\rho}_A = \mathrm{Tr}_B[\hat{\rho}], \tag{2.16}$$

as a reduced density operator, applying the trace, Tr_B, over the system density operator $\hat{\rho}$.

In the case that both sub-systems $\mathcal{A}$ and $\mathcal{B}$ are independent (uncorrelated), the density operator of the system,

$$\hat{\rho} = \hat{\rho}_A \otimes \hat{\rho}_B, \tag{2.17}$$

could be written as a tensorial product of,

$$\hat{\rho}_A = \sum_{a,a'} \rho_{a,a'} |a\rangle \langle a'|, \qquad \hat{\rho}_B = \sum_{b,b'} \rho_{b,b'} |b\rangle \langle b'|, \tag{2.18}$$

the density operators in sub-systems A and B, respectively.

2.1.4 Thermal-equilibrium density operators

The classical density-distribution function for an statistical ensemble has a correspondence with the density operator when we compute the average of observables. Therefore, how is expected, the density operator $\hat{\rho}$ could represent statistical ensembles [Greiner et al., 2012, Nolting et al., 2018].

The evolution of an observable $\langle \hat{\mathcal{A}} \rangle$, based in definition in Eq. (2.8) and Liouville's equation (2.9), is given by,

$$\frac{d}{dt} \langle \hat{\mathcal{A}} \rangle = -i \langle [\hat{\mathcal{H}}, \hat{\mathcal{A}}] \rangle, \tag{2.19}$$

No matter the form of $\hat{\mathcal{A}}$, for obtaining an stationary ensemble, it is, where the average observables does not evolve, is necessary,

$$\frac{d}{dt} \langle \hat{\mathcal{A}} \rangle = 0 \longrightarrow [\hat{\mathcal{H}}, \hat{\rho}] = 0, \tag{2.20}$$

which imposes that $\hat{\rho}$ commute with $\hat{\mathcal{H}}$. The restriction in Eq. (2.20) could be satisfied when the density operator $\hat{\rho} = \hat{\rho}(\hat{\mathcal{H}})$ is a function of $\hat{\mathcal{H}}$, which happens for the following ensembles.

Canonical density operator

For a system at fixed temperature T, volume V and number of particle N, the canonical ensemble describes the system through the density operator,

$$\hat{\rho}_{\mathrm{Can}} = \frac{e^{-\beta \hat{\mathcal{H}}}}{Z}, \qquad Z = \mathrm{Tr}[e^{-\beta \hat{\mathcal{H}}}], \tag{2.21}$$

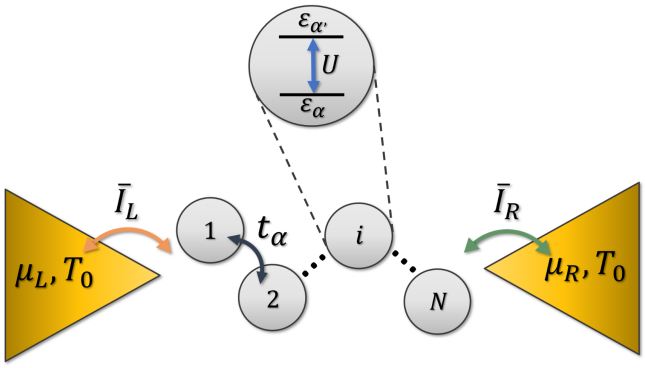

Figure 2.2: Model of nanojunction where a nano-sized material is placed between two leads. The nano-sized material is modelled as a conducting array based in N sites where electrons could hopping at rate t_α between the local energy levels ε_α, and Coulomb interaction U appears for electrons between different local energy levels ε_α and $\varepsilon_{\alpha'}$. When a bias voltage is applied, the split of the lead chemical potentials, μ_L and μ_R, induces electron transference at the interfases, measured as an stationary electron current $\bar{I}_L$ and $\bar{I}_R$.

where $\beta = (k_B T)^{-1}$ with k_B the Boltzmann constant, and Z is the canonical partition function. This definition ensures the condition of stationary ensemble in Eq. (2.20).

Grand-canonical density operator

For a system at fixed temperature T, volume V and chemical potential μ, the grand-canonical ensemble describes the system through density operator,

$$\hat{\rho}_{\mathrm{GCan}} = \frac{e^{-\beta(\hat{\mathcal{H}}-\mu\hat{\mathcal{N}})}}{\mathcal{Z}}, \qquad \mathcal{Z} = \mathrm{Tr}[e^{-\beta(\hat{\mathcal{H}}-\mu\hat{\mathcal{N}})}], \tag{2.22}$$

where $\hat{\mathcal{N}}$ is the number operator and $\mathcal{Z}$ is the grand-canonical partition function. This definition ensures the condition of stationary ensemble in Eq. (2.20).

2.2 Model of nanojuction

The modelled nanojunction is described by the Hamiltonian,

$$\hat{\mathcal{H}} = \hat{\mathcal{H}}_C + \hat{\mathcal{H}}_E + \hat{\mathcal{H}}_I, \tag{2.23}$$

where the nano-sized material, described by $\hat{\mathcal{H}}_C$, interact with an environment, described by $\hat{\mathcal{H}}_E$, through a interaction Hamiltonian $\hat{\mathcal{H}}_I$. Because the nano-sized material and the environment are composed by many-particles systems, an easy and compact way for describing them is use the second quantization theory, where the Hamiltonians are written in terms creation and annihilation operators [Bruus and Flensberg, 2004, Mahan, 2013].

2.2.1 Second quantization theory

A N-particle system could be described in the Fock space through to the Fock state,

$$|n_1, n_2, ...\rangle\,, \qquad \sum_\alpha n_\alpha = N, \tag{2.24}$$

where the number n_α in the Fock state represents the number of particles in the state (orbital) ϕ_α of the system, while right condition ensures the system contains N particles. The Fock states $\{|n_1, n_2, ...\rangle\}$ define an orthonormal basis, it is,

$$\langle n_1, n_2, ...|n_1^`, n_2^`, ...\rangle = \delta_{n_1,n_1^`}\delta_{n_2,n_2^`}..., \tag{2.25}$$

where δ is a Kronecker delta.
In the second quantization theory is defined $\hat{n}_\alpha$, the local number operator of particles in the state ϕ_α, which, applied in a Fock state,

$$\hat{n}_\alpha |..., n_{\alpha-1}, n_\alpha, n_{\alpha+1}...\rangle = n_\alpha |..., n_{\alpha-1}, n_\alpha, n_{\alpha+1}...\rangle , \tag{2.26}$$

obtains n_α as an eigenvalue. Based in local number operators in Eq. (2.26), is defined the (total) number operator as,

$$\hat{\mathcal{N}} = \sum_\alpha \hat{n}_\alpha, \tag{2.27}$$

which, applied in a Fock state, obtains the number of particles N as an eigenvalue.

Bosons

For bosons, the number of particles per state, $n_\alpha = \{0, 1, 2, ...\}$, is restricted to non-negative numbers, while the local number operator is defined as $\hat{n}_\alpha = \hat{a}_\alpha^\dagger \hat{a}_\alpha$, where the operators $\hat{a}_\alpha$ and $\hat{a}_\alpha^\dagger$ annihilates and creates, respectively, a boson in the state α, according to,

$$\begin{aligned} \hat{a}_\alpha |..., n_{\alpha-1}, n_\alpha, n_{\alpha+1}...\rangle &= \sqrt{n_\alpha} |..., n_{\alpha-1}, n_\alpha - 1, n_{\alpha+1}, ...\rangle , \\ \hat{a}_\alpha^\dagger |...n_{\alpha-1}, n_\alpha, n_{\alpha+1}, ...\rangle &= \sqrt{n_\alpha + 1} |..., n_{\alpha-1}, n_\alpha + 1, n_{\alpha+1}, ...\rangle , \end{aligned} \tag{2.28}$$

which, because the symmetry permutation of the boson-wave function, respects the commutation rules,

$$[\hat{a}_\alpha, \hat{a}_\beta] = 0, \qquad \left[\hat{a}_\alpha^\dagger, \hat{a}_\beta^\dagger\right] = 0, \qquad \left[\hat{a}_\alpha, \hat{a}_\beta^\dagger\right] = \delta_{\alpha,\beta}, \tag{2.29}$$

Fermions

For Fermions, the number of particles per state, $n_\alpha = \{0, 1\}$, is restricted to that two values, while the local number operator is defined as $\hat{n}_\alpha = \hat{c}_\alpha^\dagger \hat{c}_\alpha$, where the operators $\hat{c}_\alpha$ and $\hat{c}_\alpha^\dagger$ annihilates and creates, respectively, a fermion in the state α, according to,

$$\begin{aligned} \hat{c}_\alpha |..., n_{\alpha-1}, 0_\alpha, n_{\alpha+1}, ...\rangle = 0 = \hat{c}_\alpha^\dagger |..., n_{\alpha-1}, 1_\alpha, n_{\alpha+1}, ...\rangle , \\ \hat{c}_\alpha |..., n_{\alpha-1}, 1_\alpha, n_{\alpha+1}, ...\rangle = |..., n_{\alpha-1}, 0_\alpha, n_{\alpha+1}, ...\rangle , \\ \hat{c}_\alpha^\dagger |..., n_{\alpha-1}, 0_\alpha, n_{\alpha+1}, ...\rangle = |..., n_{\alpha-1}, 1_\alpha, n_{\alpha+1}, ...\rangle , \end{aligned} \tag{2.30}$$

which, because the anti-symmetry permutation in the fermion-wave function, respects the anti-commutation rules,

$$\{\hat{c}_\alpha, \hat{c}_\beta\} = 0, \qquad \{\hat{c}_\alpha^\dagger, \hat{c}_\beta^\dagger\} = 0, \qquad \{\hat{c}_\alpha, \hat{c}_\beta^\dagger\} = \delta_{\alpha,\beta}, \tag{2.31}$$

where $\{\hat{c}_\alpha, \hat{c}_\beta\} = \hat{c}_\alpha \hat{c}_\beta + \hat{c}_\beta \hat{c}_\alpha$ is the anticommutator.

Operators

In a N-particle system, a one-particle operator $\hat{\mathcal{O}}_1$ and a two-particle operator $\hat{\mathcal{O}}_2$ have a form,

$$\hat{\mathcal{O}}_1 = \sum_{s=1}^{N} \hat{T}_s, \qquad \hat{\mathcal{O}}_2 = \sum_{s \neq s,}^{N} \hat{V}_{s,s,}, \tag{2.32}$$

where the operator $\hat{T}_s \equiv T(\vec{r}_s)$ acts over the particle s at position $\vec{r}_s$, while the operator $\hat{V}_{s,s,} \equiv V(\vec{r}_s, \vec{r}_{s,})$ acts over the particle s and $s,$ at positions $\vec{r}_s$ and $\vec{r}_s$, respectively.
In the second quantization theory, the operators in Eq. (2.32) could be written as,

$$\begin{aligned} \hat{\mathcal{O}}_1 &= \sum_{\alpha,\alpha,} T_{\alpha\alpha,} \hat{u}_\alpha^\dagger \hat{u}_{\alpha,}, \qquad T_{\alpha\alpha,} = \int \phi_\alpha^*(\vec{r}) T(\vec{r}) \phi_{\alpha,}(\vec{r}) d\vec{r}, \\ \hat{\mathcal{O}}_2 &= \sum_{\alpha,\alpha,,\beta,\beta,} V_{\alpha\alpha,\beta\beta,} \hat{u}_\alpha^\dagger \hat{u}_{\alpha,}^\dagger \hat{u}_{\beta,} \hat{u}_\beta, \qquad V_{\alpha\alpha,\beta\beta,} = \int \phi_\alpha^*(\vec{r}) \phi_{\alpha,}^*(\vec{r}) V(\vec{r},\vec{r}) \phi_\beta(\vec{r}) \phi_{\beta,}(\vec{r}) d\vec{r} d\vec{r}, \end{aligned} \tag{2.33}$$

where $\hat{u}_\alpha^\dagger$ and $\hat{u}_\alpha$ are the creation and annihilation operators, respectively, of either fermions or bosons at the state ϕ_α.

2.2.2 Conducting array

The nano-sized material, either quantum dots or single molecules, attached to the leads is modelled as a conducting array of N sites and α local energy levels per site, as is shown in Fig. 2.2, where an isolated electron in the site i and local energy level α is described by the atomic-like orbital wave function $\phi_{i,\alpha}$ and has a (local) energy ε_α^i. For a system of S interacting electrons with equal mass m_e and charge e in the conducting array, the Hamiltonian is,

$$\hat{\mathcal{H}}_C = \sum_{s \in S} \left(\frac{\vec{p}_s{}^2}{2m_e} + V(\vec{r}_s) \right) + \frac{1}{2} \sum_{s \neq s, \in S} \frac{e^2}{|\vec{r}_s - \vec{r}_{s,}|}, \tag{2.34}$$

where the first summation correspond to the kinetic energy and the ion-core potential of an isolated electron s, and the second summation correspond to the Coulomb interaction between electrons s and $s,$.
The conducting array Hamiltonian in Eq. (2.34) in the second quantization theory, based in Eq. (2.33), is described by fermionic creation and annihilation operators, $\hat{c}_{i,\alpha}^\dagger$ and $\hat{c}_{i,\alpha}$, respectively, of electrons in the site i and orbital $\phi_{i,\alpha}$ of the conducting array as [Hubbard, 1963, Hubbard, 1967][1],

$$\hat{\mathcal{H}}_C = \sum_{i,j} \sum_{\alpha,\alpha,} T_{\alpha\alpha,}^{ij} \hat{c}_{i,\alpha}^\dagger \hat{c}_{j,\alpha,} + \frac{1}{2} \sum_{i,j,k,l} \sum_{\alpha,\alpha,,\beta,\beta,} I_{ijkl}^{\alpha\alpha,\beta\beta,} \hat{c}_{i,\alpha}^\dagger \hat{c}_{j,\alpha,}^\dagger \hat{c}_{l,\beta,} \hat{c}_{k,\beta}, \tag{2.35}$$

[1] In the following, the spin degree of freedom of electron is not considered, but it could be taking in to account adding an index $\sigma = \{\downarrow, \uparrow\}$ in the fermionic operators.

where is defined,

$$\begin{aligned} T^{ij}_{\alpha\alpha'} &= \int \phi^*_{i,\alpha}(\vec{r}) \left(\frac{\vec{p}^2}{2m_e} + V(\vec{r}) \right) \phi_{j,\alpha'}(\vec{r}) d\vec{r}, \\ I^{ijkl}_{\alpha\alpha',\beta\beta'} &= \int \phi^*_{i,\alpha}(\vec{r}) \phi^*_{j,\alpha'}(\vec{r}') \left(\frac{e^2}{|\vec{r} - \vec{r}'|} \right) \phi_{k,\beta}(\vec{r}) \phi_{l,\beta'}(\vec{r}') d\vec{r} d\vec{r}', \end{aligned} \tag{2.36}$$

the hopping and the coulomb interaction integral, respectively. The hopping and the coulomb integrals in Eq. (2.36) are approximated to,

$$\begin{aligned} T^{ij}_{\alpha\alpha'} &= \varepsilon^i_\alpha \delta_{\alpha,\alpha'} \delta_{i,j} + t^{i,j}_\alpha \delta_{\alpha,\alpha'} (\delta_{j,i+1} + \delta_{i,j+1}), \\ I^{ijkl}_{\alpha\alpha',\beta\beta'} &= U^i_{\alpha,\alpha'} \delta_{j,i} \delta_{l,i} \delta_{k,j} \delta_{\beta',\alpha} \delta_{\beta,\alpha'}, \end{aligned} \tag{2.37}$$

where the hopping integral describes the local energy ε^i_α and electron hopping between the the site i and $i+1$ in the local level ϕ_α at rate $t^{i,i+1}_\alpha$, while the coulomb integral describes repulsion between electrons in the same site i at different local levels ϕ_α and $\phi_{\alpha'}$ with an associated energy $U^i_{\alpha,\alpha'}$. Using the approximation in Eq.(2.37), the conducting array Hamiltonian in Eq. (2.35) is reduced to,

$$\hat{\mathcal{H}}_C = \sum_i \left(\sum_\alpha \varepsilon_\alpha \hat{c}^\dagger_{i,\alpha} \hat{c}_{i,\alpha} + \frac{U}{2} \sum_{\alpha' \neq \alpha} \hat{c}^\dagger_{i,\alpha'} \hat{c}_{i,\alpha'} \hat{c}^\dagger_{i,\alpha} \hat{c}_{i,\alpha} + \sum_\alpha t_\alpha \left(\hat{c}^\dagger_{i,\alpha} \hat{c}_{i+1,\alpha} + \hat{c}^\dagger_{i+1,\alpha} \hat{c}_{i,\alpha} \right) \right), \tag{2.38}$$

where was considered equals local energies, $\varepsilon^i_\alpha \equiv \varepsilon_\alpha$, Coulomb energies, $U^i_{\alpha,\alpha'} \equiv U$, and hopping rates, $t^{i,i+1}_\alpha \equiv t_\alpha$. In the case of circular conducting array, the overlapping between the site $i = 1$ and the site $i = N$ produce a non-zero hopping constant t_α between these sites, subject to the boundary condition $N + 1 = 1$.

The conducting array Hamiltonian in Eq. (2.38) could be written in diagonal form as,

$$\hat{\mathcal{H}}_C = \sum_n \omega_n |e_n\rangle \langle e_n| \tag{2.39}$$

where $\{\omega_n\}$ is the conducting array spectrum and $\{|e_n\rangle\}$ are conducting array eigenstates. In the case of N sites and α local energy levels, the number of eigenstates will be $2^{N \times \alpha}$, which increases exponentially. Is expected the hopping rate t_α produces eigenstates which looks as a linear combination of electrons at different sites of the conducting array (delocalization), which induce the conducting array behaves as a large single site [Yoffe, 2001].
Despite the approximation done for the conducting array Hamiltonian in Eq. (2.38), in principle other approximations could be done, because the nanojunction dynamics (discussed in Chapter 3) consider the conducting array Hamiltonian in diagonal form as Eq. (2.39), which ensures that internal interactions are taken into account [Pedersen and Wacker, 2005, Esposito and Galperin, 2009].

2.2.3 Environment

The environment is composed by different reservoirs, these are the leads ($\{L, R\}$), the radiation (rad) and thermalized phonons (ph), described by the Hamiltonian,

$$\hat{\mathcal{H}}_E = \sum_{\lambda=\{L,R,\mathrm{rad},\mathrm{ph}\}} \hat{\mathcal{H}}_\lambda, \tag{2.40}$$

as a sum of individual Hamiltonian $\hat{\mathcal{H}}_\lambda$ of the reservoir λ. Considering thermal equilibrium reservoirs, they are described by thermal equilibrium density operators discussed in Sec. 2.1.4.

Leads

Considering a lead $l = \{L, R\}$ like a electron-gas reservoir, it means free electrons, with well defined temperature T, volume V and chemical potential μ_l, the Hamiltonian is,

$$\hat{\mathcal{H}}_l = \sum_s \frac{\vec{p}_s{}^2}{2m_e}, \tag{2.41}$$

with eigenfunctions and energies,

$$\phi_{\vec{k}}(\vec{r}) = \frac{1}{\sqrt{V}} e^{i\vec{k}\cdot\vec{r}}, \qquad \omega_{\vec{k}} = \frac{\vec{k}^2}{2m_e}, \tag{2.42}$$

respectively. In the second quantization theory, the lead Hamiltonian in Eq. (2.41), using the Eq. (2.33) and Eq. (2.42), becomes,

$$\hat{\mathcal{H}}_l = \sum_{\vec{k}} \omega_{\vec{k}} \hat{c}^\dagger_{l,\vec{k}} \hat{c}_{l,\vec{k}}, \tag{2.43}$$

where $\hat{c}_{l,\vec{k}}$ ($\hat{c}^\dagger_{l,\vec{k}}$) annihilates (creates) one electron in the lead l in the mode $\vec{k}$.

Based in grand-canonical density operator in Eq. (2.22) and Hamiltonian in Eq. (2.43), the thermal-equilibrium leads are described by,

$$\hat{\rho}_l = \frac{\exp\left(-\beta_0(\hat{\mathcal{H}}_l - \mu_l\hat{\mathcal{N}}_l)\right)}{\mathrm{Tr}_l\left[\exp\left(-\beta_0(\hat{\mathcal{H}}_l - \mu_l\hat{\mathcal{N}}_l)\right)\right]}, \qquad \hat{\mathcal{H}}_l = \sum_k \omega_k \hat{c}^\dagger_{l,k}\hat{c}_{l,k}, \qquad \hat{\mathcal{N}}_l = \sum_k \hat{c}^\dagger_{l,k}\hat{c}_{l,k}, \tag{2.44}$$

where $\beta_0 = (k_B T_0)^{-1}$ at room temperature T_0, μ_l the chemical potential, $\hat{\mathcal{H}}_l$ the number operator and Tr_l is the trace over the degrees of freedom of the lead l.

Radiation

The Maxwell equations describe the radiation in the free space by the electric field $\vec{E}$ and the magnetic field $\vec{B}$. In the Coulomb gauge, both fields are computed through the potential vector $\vec{A}$ as,

$$\vec{E} = -\frac{1}{c}\frac{\partial \vec{A}}{\partial t}, \qquad \vec{B} = \vec{\nabla} \times \vec{A}, \tag{2.45}$$

where c is the speed of light.
Considering radiation in a homogeneous space with lineal polarization $\vec{\sigma}_k$ in a volume V, the potential vector is reduced to [Nitzan, 2006],

$$\hat{\vec{A}} = c\sum_{\vec{k}} \sqrt{\frac{2\pi}{\epsilon_0 V \omega_{\vec{k}}}} \left(\hat{a}_{\mathrm{rad},\vec{k}} \exp\left(i(\vec{k}\cdot\vec{r} - \omega_{\vec{k}} t)\right) + \hat{a}^{\dagger}_{\mathrm{rad},\vec{k}} \exp\left(-i(\vec{k}\cdot\vec{r} - \omega_{\vec{k}} t)\right)\right) \vec{\sigma}_k, \tag{2.46}$$

where ϵ_0 is the permittivity of free space, and $\hat{a}_{\mathrm{rad},\vec{k}}$ and $\hat{a}^{\dagger}_{\mathrm{rad},\vec{k}}$ are bosonic creation and annihilation operators, respectively, of photons in the mode $\vec{k}$. Whit the fields defined in Eq. (2.45) and the vector potential in Eq. (2.46), the energy of radiation is reduced to,

$$\hat{\mathcal{H}}_{\mathrm{rad}} = \sum_{\vec{k}} \omega_{\vec{k}} \left(\hat{a}^{\dagger}_{\mathrm{rad},\vec{k}} \hat{a}_{\mathrm{rad},\vec{k}} + \frac{1}{2} \right), \tag{2.47}$$

where $\omega_{\vec{k}}$ is the energy of the mode $\vec{k}$.

Based in canonical-density operator in Eq. (2.21) and Hamiltonian in Eq. (2.47), the radiation is described by,

$$\hat{\rho}_{\mathrm{rad}} = \frac{\exp\left(-\beta_0 \hat{\mathcal{H}}_{\mathrm{rad}}\right)}{\mathrm{Tr}_{\mathrm{rad}}\left[\exp\left(-\beta_0 \hat{\mathcal{H}}_{\mathrm{rad}}\right)\right]}, \qquad \hat{\mathcal{H}}_{\mathrm{rad}} = \sum_p \omega_p \hat{a}^{\dagger}_{\mathrm{rad},p} \hat{a}_{\mathrm{rad},p}, \tag{2.48}$$

where $\mathrm{Tr}_{\mathrm{rad}}$ is the trace over the degrees of freedom of the radiation.

Phonons

Considering a group of N atomic-ion cores with equal mass m_N at the site of the conducting array. If they are connected by a elastic constant K, they are be described by the Hamiltonian [Scheer and Cuevas, 2017],

$$\hat{\mathcal{H}}_{\mathrm{ph}} = \sum_i \frac{P_i^2}{2m_N} + \frac{K}{2} \sum_i (R_i - R_{i-1})^2, \tag{2.49}$$

where P_i and R_i are the momentum and the position of the i-th atomic-ion core. Applying a Fourier transform, the canonical variables R_i and P_i becomes,

$$R_k = \frac{1}{\sqrt{N}} \sum_j R_j \exp\left(-ikaj\right), \qquad P_k = \frac{1}{\sqrt{N}} \sum_j P_j \exp\left(ikaj\right), \tag{2.50}$$

where a is the distance between cores and the commutation relation $[R_k, P_k] = i\delta_{k,k}$ is preserved also in the k-space.
Based in the Fourier transform in Eq. (2.50), the phonon Hamiltonian in Eq. (2.49) could be written as,

$$\hat{\mathcal{H}}_{\mathrm{ph}} = \sum_k \frac{1}{2m_N} P_k P_{-k} + \sum_k \frac{m_N \omega_k}{2} R_k R_{-k}, \qquad \omega_k = \frac{4K}{m_N} \sin^2\left(\frac{ka}{2}\right), \tag{2.51}$$

where ω_k is the energy in the mode k. Defining,

$$\hat{a}_{\mathrm{ph},k} = \sqrt{\frac{m_N\omega_k}{2}}\left(R_k + \frac{i}{m_N\omega_k}P_{-k}\right), \qquad \hat{a}^\dagger_{\mathrm{ph},k} = \sqrt{\frac{m_N\omega_k}{2}}\left(R_{-k} - \frac{i}{m_N\omega_k}P_k\right), \tag{2.52}$$

the creation and annihilation operators, respectively, of phonon in the mode k, the phonon Hamiltonian in Eq. (2.51) could be easily written in the second quantization theory as,

$$\hat{\mathcal{H}}_{\mathrm{ph}} = \sum_k \omega_k \left(\hat{a}^\dagger_{\mathrm{ph},k}\hat{a}_{\mathrm{ph},k} + \frac{1}{2}\right). \tag{2.53}$$

Based in canonical-density operator in Eq. (2.21) and Hamiltonian in Eq. (2.53), the thermalized phonons are described by,

$$\hat{\rho}_{\mathrm{ph}} = \frac{\exp\left(-\beta_0\hat{\mathcal{H}}_{\mathrm{ph}}\right)}{\mathrm{Tr}_{\mathrm{ph}}\left[\exp\left(-\beta_0\hat{\mathcal{H}}_{\mathrm{ph}}\right)\right]}, \qquad \hat{\mathcal{H}}_{\mathrm{ph}} = \sum_q \omega_q \hat{a}^\dagger_{\mathrm{ph},q}\hat{a}_{\mathrm{ph},q}, \tag{2.54}$$

where $\mathrm{Tr}_{\mathrm{ph}}$ is the trace over the degrees of freedom of the phonons ph.

2.2.4 Interactions

All the reservoirs interact with the conducting array, defining a total interaction,

$$\hat{\mathcal{H}}_I = \sum_{\lambda=\{L,R,\mathrm{rad},\mathrm{ph}\}} \hat{\mathcal{H}}^\lambda_I, \tag{2.55}$$

as a sum of individual system-reservoir interaction $\hat{\mathcal{H}}^\lambda_I$ of the reservoir λ and the conducting array. Through the interactions, the thermodynamic parameters of the reservoirs induces non-equilibrium dynamics in the conducting array.

Lead tunneling

When the lead $l = \{L, R\}$ is next to the conducting array, the overlapping of the electronic wave functions produce electron transference between them, described by the Hamiltonian,

$$\hat{\mathcal{H}}^l_I = \sum_{i,\alpha,k}\left(V^{\alpha k}_{il}\hat{c}^\dagger_{i,\alpha}\hat{c}_{l,k} + (V^{\alpha k}_{il})^*\hat{c}^\dagger_{l,k}\hat{c}_{i,\alpha}\right), \tag{2.56}$$

as a tunneling process [Scheer and Cuevas, 2017], where $V^{\alpha k}_{il}$ is the coupling constant between an electron in the lead l in the mode k and an electron in the conducting array site i and local energy level α. The interaction Hamiltonian in Eq. (2.56) does not include the energy (exciton) transference with the leads, which is an operator of fourth order in fermion operators and acts as a non-radiative de-excitation of the conducting array through the creation of a electron-hole pair in the leads [Galperin and Nitzan, 2005, Galperin and Nitzan, 2006]. It has been assumed that the coupling constant,

$$V^{\alpha k}_{il} = u^{(l)}_i V^{(l)}_k, \tag{2.57}$$

could be divided in a conducting array term, $u_i^{(l)} \in \mathbb{R}$, and a reservoir part, $V_k^{(l)} \in \mathbb{C}$.
With the coupling approximation in Eq. (2.57), the interaction Hamiltonian in Eq. (2.56) becomes,

$$\hat{\mathcal{H}}_I^l = \sum_{i,\alpha,k} u_i^{(l)} \left(V_k^{(l)} \hat{c}_{i,\alpha}^\dagger \hat{c}_{l,k} + V_k^{(l)*} \hat{c}_{l,k}^\dagger \hat{c}_{i,\alpha} \right), \tag{2.58}$$

where the conducting array dependence,$u_i^{(l)}$, is modelled as a Kronecker delta function whit value 1 when the conducting array site i is the nearest site to the lead l, because is where the coupling is highest.

Light-matter interaction

The interaction between the radiation and the conducting array, up to the dipolar approximation, is given by [Nitzan, 2006],

$$\hat{\mathcal{H}}_I^{\text{rad}} = -\sum_s \hat{\vec{\mu}}_s \cdot \hat{\vec{E}}(\vec{r}_s), \tag{2.59}$$

where $\hat{\vec{\mu}}_s$ is the dipole operator of an electron s of the conducting array and $\hat{\vec{E}}(\vec{r}_s)$ is the electric field in the Schrödinger picture at the position $\vec{r}_s$ of an electron s. Considering the radiation wavelength greater than the conducting array length, the electric field $\hat{\vec{E}}(\vec{r}=0)$ is spatially constant, defining $\vec{r}=0$ at the beginning of the conducting array.
In the second quantization theory, applying the Eq. (2.33), the dipole operator could be written as,

$$\sum_s \hat{\vec{\mu}}_s = \sum_i \sum_{\alpha \neq \alpha'} \vec{\mu}_i^{\alpha\alpha'} \hat{c}_{i,\alpha}^\dagger \hat{c}_{i,\alpha'}, \qquad \vec{\mu}_i^{\alpha\alpha'} = \int \phi_{i,\alpha}^*(\vec{r}) \hat{\vec{\mu}}(\vec{r}) \phi_{i,\alpha'}(\vec{r}) d\vec{r}, \tag{2.60}$$

where $\vec{\mu}_i^{\alpha\alpha'}$ is the dipole integral. In Eq. (2.60) has been considered only dipole transitions between the different levels at the same site, ignoring excimer formation[2] and permanent dipole moments. Considering the dipole operator in Eq. (2.60) and the electric field defined in Eq. (2.45), the interaction Hamiltonian in Eq. (2.59), under the rotating-wave approximation (RWA), becomes,

$$\hat{\mathcal{H}}_I^{\text{rad}} = \sum_{i,\alpha>\alpha',p} u_i^{(\text{rad})} \left(V_p^{(\text{rad})} \hat{c}_{i,\alpha}^\dagger \hat{c}_{i,\alpha'} \hat{a}_{\text{rad},p} + V_p^{(\text{rad})*} \hat{c}_{i,\alpha'}^\dagger \hat{c}_{i,\alpha} \hat{a}_{\text{rad},p}^\dagger \right), \tag{2.61}$$

where has been considered the dipole operator aligned in the electric field polarization and has been assumed the coupling constant,

$$u_i^{(\text{rad})} V_p^{(\text{rad})} = -i \sqrt{\frac{2\pi\omega_p}{\epsilon_0 V}} \mu_i^{\alpha\alpha'}, \tag{2.62}$$

could be divided in a conducting array term, $u_i^{(\text{rad})} \in \mathbb{R}$, and a reservoir part, $V_p^{(\text{rad})} \in \mathbb{C}$. The conducting array dependence, $u_i^{(\text{rad})} = 1$, is modelled as a constant with value for all the conducting array sites, because are considered the dipoles operators equals for all the conducting array sites.

[2] Transitions between between different conducting array sites.

Electron-phonon interaction

The interaction between electrons in the conducting array and the atomic-ion cores is described by the Hamiltonian,

$$\hat{\mathcal{H}}_I^{\mathrm{ph}} = \sum_{s,i} V(r_s - R_i), \tag{2.63}$$

where $V(r_s - R_i)$ is a potential of an electron s and an atomic-ion core i. Expanding the potential respect to the equilibrium position R_i^0 of the atomic-ion cores, up to first order in the Taylor expansion the Hamiltonian interaction in Eq. (2.63) becomes [Mahan, 2013],

$$\begin{aligned} \hat{\mathcal{H}}_I^{\mathrm{ph}} &= -\sum_{s,i} Q_i \frac{\partial}{\partial R_i} V(r_s - R_i)|_{R_i = R_i^0}, \\ Q_i = R_i - R_i^0 &= \frac{1}{\sqrt{N}} \sum_q \sqrt{\frac{1}{2 m_N \omega_q}} \left(\hat{a}_{\mathrm{ph},q} + \hat{a}_{\mathrm{ph},-q}^{\dagger} \right) \exp\left(i q R_i^0 \right), \end{aligned} \tag{2.64}$$

where Q_i, is the displacement operator in terms of photon creation and annihilation operator defined in Eq. (2.52).
Writing the potential $V(r_s - R_n)$ in Fourier transform as,

$$V(r_s - R_i) = \frac{1}{\sqrt{N}} \sum_k V_k \exp\left(i k (r_s - R_i) \right), \tag{2.65}$$

the Hamiltonian in Eq. (2.64) is reduced to,

$$\hat{\mathcal{H}}_I^{\mathrm{ph}} = \sum_{s,q} g_{s,q} \left(\hat{a}_{\mathrm{ph},q} + \hat{a}_{\mathrm{ph},-q}^{\dagger} \right), \qquad g_{s,q} = i \sqrt{\frac{1}{2 m_N \omega_q}} q V_q \exp\left(i q r_s \right), \tag{2.66}$$

where $g_{s,q}$ is a one-electron operator, which, written in second quantization theory using Eq. (2.33), becomes,

$$\sum_s g_{s,q} = \sum_i \sum_\alpha u_i^{(\mathrm{ph})} V_q^{(\mathrm{ph})} \hat{c}_{i,\alpha}^{\dagger} \hat{c}_{i,\alpha}, \qquad u_i^{(\mathrm{ph})} V_q^{(\mathrm{ph})} = \int \phi_{i,\alpha}^*(\vec{r}) g_q \phi_{i,\alpha}(\vec{r}) d\vec{r}, \tag{2.67}$$

where has been supposed the integral have non-zero coupling constant, $u_i^{(\mathrm{ph})} V_q^{(\mathrm{ph})}$, only for electron in the same site and energy level [Gauger et al., 2008] and coupling constant is divided in a conducting array term, $u_i^{(\mathrm{rad})} \in \mathbb{R}$, and a reservoir part, $V_q^{(\mathrm{rad})} \in \mathbb{C}$.
With the coupling constant approximation in Eq. (2.67), the Hamiltonian interaction in Eq. (2.66) is reduced to,

$$\hat{\mathcal{H}}_I^{\mathrm{ph}} = \sum_{i,\alpha,q} u_i^{(\mathrm{ph})} V_q^{(\mathrm{ph})} \hat{c}_{i,\alpha}^{\dagger} \hat{c}_{i,\alpha} \left(\hat{a}_{\mathrm{ph},q} + \hat{a}_{\mathrm{ph},q}^{\dagger} \right), \tag{2.68}$$

where is modelled the conducting array dependence, $u_i^{(\mathrm{ph})} = (-1)^{i+1}$, because it taking in to account a relative phase of π of the conducting array sites for a longitudinal mode in coupling of Eq. (2.66) [Sowa et al., 2017].

Chapter 3

Nanojunction dynamics

Many theoretical methods has been developed for treating the dynamics of non-equilibrium systems as the nanojuction described in Sec. 2.2. Considering the non-equilibrium system as a open-quantum system, the density operator formalism, discussed in Sec. 2.1, is capable to derive a quantum master equation for the system dynamics under a set of approximations and assumptions. Despite quantum master equations do not provide exact dynamics, they have been applied to chemical and physical problems due its intuitive results and easy implementation.
In the following Chapter is derived the nanojunction dynamics though a quantum master equation, which captures the interaction of conducting array with the environment as transition between conducting array eigenstates induced by the individual reservoirs. Based in the nanojunction dynamics, is derived an expression for the electron current through the molecule, and it is explained the implementation for obtaining the typical current-voltage curve for characterizing the electron transport in nanojuntions.

3.1 Quantum master equation

The model considers the nanojunction as an open-quantum system, where the conducting array is a quantum system which interacts with an environment composed by different reservoirs, as is shown in Fig. 3.1(a). Therefore, the nanojunction is described by the density operator $\hat{\rho}$, containing information about the conducting array, through the reduced density operator $\hat{\rho}_C = \mathrm{Tr}_E\left[\hat{\rho}\right]$, and the environment, through the reduced density operator $\hat{\rho}_E = \mathrm{Tr}_C\left[\hat{\rho}\right]$.

Considering weak coupling of the system-reservoir interactions, the interaction Hamiltonian, $\hat{\mathcal{H}}_I$, is considered through perturbation theory in the nanojunction dynamics. It means the environment and conducting array evolves as uncorrelated sub-systems. Considering also the environment is bigger than the conducting array (Born approximation), the nanojunctions density operator,

$$\hat{\rho}(t) = \hat{\rho}_C(t) \otimes \hat{\rho}_E, \tag{3.1}$$

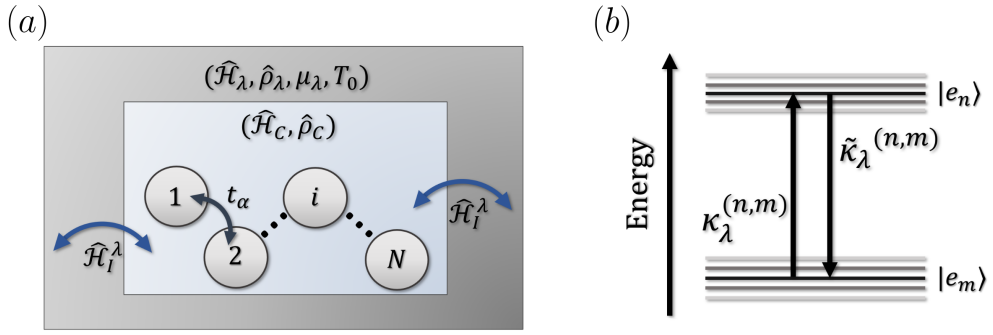

Figure 3.1: (a) Open-quantum system picture, where the conducting array, described by $(\hat{\mathcal{H}}_C, \hat{\rho}_C)$, interact with a reservoir λ, described by $(\hat{\mathcal{H}}_\lambda, \hat{\rho}_\lambda, \mu_\lambda, T_0)$, through an interaction Hamiltonian $\hat{\mathcal{H}}_I^\lambda$. (b) Diagram of electron transitions induced by a reservoir λ at effective transfer rate $\kappa_\lambda^{(n,m)}$ for transition between conducting array eigenstates $|e_m\rangle \to |e_n\rangle$ and at effective transfer rate $\tilde{\kappa}_\lambda^{(n,m)}$ for transition between conducting array eigenstates $|e_n\rangle \to |e_m\rangle$.

looks as a tensor product of the conducting array density operator, $\hat{\rho}_C(t)$, which evolves in function of time, and the environment density operator,

$$\hat{\rho}_E = \hat{\rho}_L \otimes \hat{\rho}_R \otimes \hat{\rho}_{\text{rad}} \otimes \hat{\rho}_{\text{ph}}, \tag{3.2}$$

which is composed by thermal-equilibrium density operators for all the reservoirs, as was discussed in Sec. 2.2.3.

Whit the last approximations, the Liouville equation for the nanojunction density operator $\hat{\rho}$ in Eq. (2.9) is reduced to the Redfield equation (derivation in Appendix A) for the conducting array dynamics,

$$\frac{d}{dt}\hat{\rho}_C(t) = -i\left[\hat{\mathcal{H}}_C, \hat{\rho}_C(t)\right] - \int_0^\infty d\tau\, \text{Tr}_E\left[\hat{\mathcal{H}}_I, \left[\hat{\mathcal{H}}_I(-\tau), \hat{\rho}_C(t)\otimes\hat{\rho}_E\right]\right], \tag{3.3}$$

where $\hat{\mathcal{H}}_I(-\tau)$ is the interaction Hamiltonian in the interaction picture at time $-\tau$. It was also considered the Markov approximation, because the reservoir correlations decay faster on time than the conducting array dynamics and is considered the environment at room temperature [Timm, 2008].

Whit the interaction Hamiltonian $\hat{\mathcal{H}}_I$ in Eq. (2.55) and the environment density operators $\hat{\rho}_E$ in Eq. (3.2), the Redfield equation in Eq. (3.3) becomes the a Lindbland quantum master equation (derivation in Appendix B),

$$\frac{d}{dt}\hat{\rho}_C(t) = -i\left[\hat{\mathcal{H}}_C, \hat{\rho}_C(t)\right] + \sum_{n,m}\left(\kappa^{(n,m)}\mathcal{L}_{n,m}\left[\hat{\rho}_C(t)\right] + \tilde{\kappa}^{(n,m)}\mathcal{L}_{m,n}\left[\hat{\rho}_C(t)\right]\right), \tag{3.4}$$

where has been defined,

$$\kappa^{(n,m)} = \sum_{\lambda=\{L,R,\text{rad},\text{ph}\}} \kappa_\lambda^{(n,m)}, \qquad \tilde{\kappa}^{(n,m)} = \sum_{\lambda=\{L,R,\text{rad},\text{ph}\}} \tilde{\kappa}_\lambda^{(n,m)}, \tag{3.5}$$

in terms of the *effective transfer rates* $\kappa_\lambda^{(n,m)}$ and $\tilde{\kappa}_\lambda^{(n,m)}$ (details in Table B.1), and the Linblandian

superoperators reads,

$$\mathcal{L}_{n,m}\left[\hat{\rho}_C(t)\right] = \hat{L}_{n,m}\hat{\rho}_C(t)\hat{L}_{n,m}^{\dagger} - \frac{1}{2}\{\hat{L}_{n,m}^{\dagger}\hat{L}_{n,m}, \hat{\rho}_C(t)\}, \qquad \hat{L}_{n,m} = |e_n\rangle\langle e_m|, \tag{3.6}$$

which guarantee positive time evolution of density operator, it is, the system conserve the probability during the evolution [Breuer et al., 2002].

The model describes the open-quantum system dynamics where the conducting array interact with a reservoir λ as electron transitions induced by the reservoir at effective transfer rate $\kappa_{\lambda}^{(n,m)}$ for transition between conducting array eigenstates $|e_m\rangle \to |e_n\rangle$ and at effective transfer rate $\tilde{\kappa}_{\lambda}^{(n,m)}$ for transition between conducting array eigenstates $|e_n\rangle \to |e_m\rangle$, as is shown in Fig. 3.1(b). The transition between eigenstates is related with the addition of subtraction of electrons when it is induced by the leads, unlike when it is induced by the radiation or thermalized phonons, which conserves the number of electrons.
The effective transfer rates, $\kappa_{\lambda}^{(n,m)}$ and $\tilde{\kappa}_{\lambda}^{(n,m)}$, depend on the conducting array transition energy $\omega_{n,m} = \omega_n - \omega_m$, and the reservoir thermodynamics parameters, as temperature T_0 and chemical potential μ_{λ}. The reservoir λ will only induce transition between eigenstates $|e_n\rangle \leftrightarrow |e_m\rangle$ is they are such that,

$$|\langle e_n|\hat{S}_{\lambda}|e_m\rangle|^2 \neq 0, \tag{3.7}$$

where $\hat{S}_{\lambda}$, defined in Table B.1, is a conducting array operator for given reservoir λ, which gives the selection rules.

Quantum master equations in the Lindbland form has been used for describing the dynamics of nanojunction [Gurvitz and Prager, 1996, Li et al., 2005, Harbola et al., 2006, Timm, 2008] because its intuitive and simple results when describe weakly coupled systems [Harbola et al., 2006, Esposito and Galperin, 2010, Thoss and Evers, 2018]. Nevertheless, the approximation typically used for deriving them sometimes becomes inadequate and leads to wrong results [Esposito and Galperin, 2010, Ballmann et al., 2012]. Because the observables are measured in stationary regime, the Markov approximation, which has been reported reaches the same results that non-Marvonian at stationary regime [Pedersen and Wacker, 2005], is not the main problem, but the perturbative treatment of coupling with the reservoir, specially at low temperature, decreases the captured transport processes [Thoss and Evers, 2018]. For example, in single molecules and carbon nanotubes quantum dots the electronic degree of freedom could be strongly coupled to an specific vibrational mode rather than the vibrational bath [Sowa et al., 2017], or the spin of electrons in quantum dots or single molecules could be strongly correlated to the spins at the leads at low temperature [Kondo, 1964]. That means that interesting transport effects, which requires a non-perturbative treatment for their description, as Franck-Condon blockade or Kondo effect for example, fall outside the scope of our model.
Many methods have arisen to describe nanojunction in a more exactly way. Some of them has performed modifications to quantum master equations, which includes non-perturbative and non-markovian [Esposito and Galperin, 2009]; taking in to account strong electron-phonon coupling, through (small) polaron transformation [Galperin et al., 2006, Galperin and Nitzan, 2006, Espos-

ito and Galperin, 2009, Sowa et al., 2017, Sowa et al., 2018]; hight order perturbation process, through Keldysh formalism [Timm, 2008]; or broadening effects of the molecular levels due to the coupling with the leads, through non-equilibrium Green functions [Pedersen and Wacker, 2005, Esposito and Galperin, 2009]. For more complex nano-sized material, interesting results has been obtained using *Ab-initio* methods, where the equilibrium electronic structure of the conducting material is taken in to account through the density of states, mixed with non-equilibrium Green functions [Taylor et al., 2002, Thoss and Evers, 2018].

3.1.1 Rate equations

From the Lindbland quantum master equation in Eq. (3.4), the population $\rho_n \equiv \rho_{n,n} = \langle e_n | \hat{\rho}_C | e_n \rangle$ at the conducting array eigenstate $|e_n\rangle$ evolves according to,

$$\frac{d}{dt}\rho_n = \sum_m \left(\kappa^{(n,m)} + \tilde{\kappa}^{(m,n)}\right)\rho_m - \rho_n \sum_m \left(\kappa^{(m,n)} + \tilde{\kappa}^{(n,m)}\right), \tag{3.8}$$

as a system of rate equations, while the coherences $\rho_{i,j} = \langle e_i | \hat{\rho}_C | e_j \rangle$ at the conducting array eigenstates $|e_i\rangle$ and $|e_j\rangle$ evolves according to,

$$\frac{d}{dt}\rho_{i,j} = -i\omega_{i,j}\rho_{i,j} - \frac{1}{2}\sum_m \left(\kappa^{(m,i)} + \kappa^{(m,j)} + \tilde{\kappa}^{(i,m)} + \tilde{\kappa}^{(j,m)}\right)\rho_{i,j}. \tag{3.9}$$

As is shown in Eq. (3.8) and (3.9), the dynamics of population and coherences are decoupled when the conducting array dynamics is written in terms of its eigenstates, because the secular approximation in the dynamics derivation [Sowa et al., 2018], what means that the whole dynamics is reduced to population transference between conducting array eigenstates with rates according to the Fermi golden rules, while the coherences decay, being zero at stationary regime [Kouwenhoven et al., 1997, Esposito and Galperin, 2010]. In principle, the decoupling could not be true if is written the density operator dynamic in other basis, for example the local basis, as in [Harbola et al., 2006].

Therefore, for solving the conducting array dynamics in Eq. (3.4), is easier to implement only the population evolutions from the rate equations in Eq. (3.8), because it reduces the system dimension from a full density operator $\hat{\rho}_C$, with $(2^{\alpha\times N})^2$ elements, to populations evolution, whit $2^{\alpha\times N}$ elements. Despite the model could obtain time dependent observables, for the system characterization the interesting observables are typically measured in the stationary regimen where the set of populations $\{\rho_n\}$ reach stationary values $\{\bar{\rho}_n\}$. Therefore, the rate equations in Eq. (3.8) are solved imposing the stationary conditions, these are,

$$\{\dot{\bar{\rho}}_n\} = 0, \qquad \sum_{n=1}^{2^{\alpha\times N}} \bar{\rho}_n = 1. \tag{3.10}$$

where the right condition ensures a non-trivial solution of the system of rates equations when the left condition is satisfied.

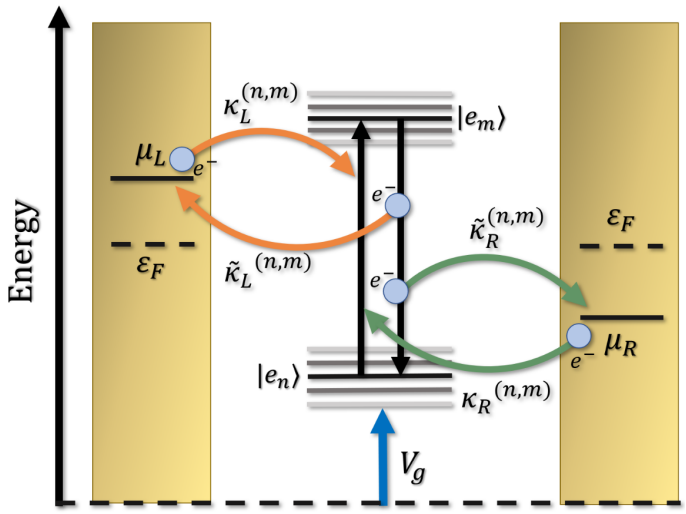

Figure 3.2: Diagram of nanojunction energy levels, where are induced electron transition between conducting array eigenstates by the leads at chemical potentials μ_L and μ_R, splitted respect to the Fermi energy ε_F because a positive bias voltage V. The presence of a gate voltage, V_g, induces an electrostatics change of the conducting array levels. Any electron transition is accompanied by an electron addition or subtraction, measured as a current I_L and I_R at the left and right interfase, respectively.

3.2 Nanojuction characterization

Because the changes of charge number by the electron transitions induced by the leads, as is shown in the Fig. 3.2, a flow (current) of electrons take place at the interfases between the conducting array and the leads, even in the stationary regime. Despite the model considers the leads are in thermal-equilibrium during all the system dynamics, the non-equilibrium dynamics of the conducting array is associated to an slightly change of the leads observables, as the number of particles, but it is not large enough to change their thermodynamics parameters (equivalent for radiation and thermalized phonon reservoirs).

3.2.1 Current-voltage

With $\hat{\mathcal{N}}_L$ and $\hat{\mathcal{N}}_R$ the number operator of electron at the left and right lead, respectively, the currents at the left and right interfases are defined as (derivation in Appendix C),

$$\begin{aligned} I_L &= -e\frac{d}{dt}\langle\hat{\mathcal{N}}_L\rangle = e\sum_{n,m}\left(\kappa_L^{(n,m)}\rho_m - \tilde{\kappa}_L^{(n,m)}\rho_n\right), \\ I_R &= e\frac{d}{dt}\langle\hat{\mathcal{N}}_R\rangle = -e\sum_{n,m}\left(\kappa_R^{(n,m)}\rho_m - \tilde{\kappa}_R^{(n,m)}\rho_n\right), \end{aligned} \tag{3.11}$$

respectively, which quantifies the variation of electrons in the leads produced by the non-equilibrium conducting array dynamics. The different sign between left and right current is associated to the definition of positive current to right direction and negative current to left direction. Giving the set of populations $\{\rho_n\}$ in function of time, the currents I_L and I_R in Eq. (3.11) could be computed in function of time too, but for characterizing the system is computed stationary currents $\bar{I}_L$ and $\bar{I}_R$, based in the set of stationary populations $\{\bar{\rho}_n\}$. Is expected in the stationary regimen $\bar{I}_L = \bar{I}_R$, because the conservation of electron number.

The contribution of an specific eigenstate $|e_n\rangle$ to the current at the left and right interfases is defined as the *state dependent current*,

$$\begin{aligned} I_L^{(n)} &= e\sum_m \left(\kappa_L^{(n,m)}\rho_m - \tilde{\kappa}_L^{(n,m)}\rho_n\right), \\ I_R^{(n)} &= -e\sum_m \left(\kappa_R^{(n,m)}\rho_m - \tilde{\kappa}_R^{(n,m)}\rho_n\right), \end{aligned} \tag{3.12}$$

at the left and the right lead interfase, respectively. In principle, the state dependent currents could satisfy $\bar{I}_L^{(n)} \neq \bar{I}_R^{(n)}$ at the stationary regime, however, because the definition in Eq. (3.11), the sum of all the state dependent currents in their respective interfases must satisfy $\sum_n \bar{I}_L^{(n)} = \sum_n \bar{I}_R^{(n)}$, because the definition in Eq. (3.11).

An external bias voltage, V, induces a change in the left and right chemical potentials, μ_L and μ_R, respectively, according to the relation,

$$\mu_L - \varepsilon_F = \varepsilon_F - \mu_R = \frac{1}{2}eV, \tag{3.13}$$

where the Fermi energy, ε_F, correspond to the common energy level for the chemical potentials at the zero bias voltage configuration, as is shown in Fig. 3.2 for a case where is applied a positive bias voltage. Is expected, if the conducting array allows it, the electrons tend to travel from lead with higher to the lower chemical potential, performing a current I_L and I_R in their respective interfases in function of time, up to reach an stationary current $\bar{I}_L$ and $\bar{I}_R$. Therefore, the applied voltage acts as a driven source of electrons through the nanojunction.
An specific region of voltage where the current modified, is measured as a peak of (differential) conductance, defined as,

$$\bar{G}_L = \frac{d\bar{I}_L}{dV}, \qquad \bar{G}_R = \frac{d\bar{I}_R}{dV}, \tag{3.14}$$

at the left and right interfase, respectively.

3.2.2 Gate voltage

Applying a gate voltage V_g through this third gate, is induced a change in the conducting energy levels as a continuous manner, as is shown in Fig. 3.2. Fixing the empty conducting array eigenstate[1] as the zero-energy reference, when the gate voltage is applied, the induced changes in the nanojuction energy levels are equivalent to a change of the Fermi energy according to,

$$\varepsilon_F \to \varepsilon_F - eV_g. \tag{3.15}$$

which decreases linearly the Fermi energy.

[1] This eigenstate represent the configuration where there is not charge in the conducting array.

Chapter 4

Results

Electron transport through quantum dots and molecular junctions, has reported interesting quantum transport phenomena. Their understanding or controlling is absolutely necessary for the possible future application as building blocks of nano-electronic devices.
In the following Chapter is described the electron transport of different nanojunctions through current-voltage curves, based in the nanojuction description given in Chapter 2 and the dynamics derived in Chapter 3. For simple conducting array, is studied the different electron transition processes induced to the conducting array by the different reservoirs, and how it affects the electron transport through the nanojunction. For more complex conducting array, based on the analysis of other interesting observables state dependent currents and photon flux, is studied the effect of the conducting array geometry in the electron transport, and the effect of an external source of incoherent pumping.

The following results has been computed using the parameters in Table 4.1. The rates γ_L,γ_R, $\gamma_{\rm rad}$ and $\gamma_{\rm ph}$ has been considered constant, ignoring their energy dependence[1]. Therefore, the main dependence of the effective transfer rates, $\kappa_\lambda^{(n,m)}$ and $\tilde{\kappa}_\lambda^{(n,m)}$, comes from the fermion or bosons densities, $f_{L(R)}^{(n,m)}$ and $n_{\rm rad(ph)}^{(n,m)}$, respectively (see details in Table B.2).
Despite the rate of spontaneous emission typically has a value of $\gamma_{\rm rad} \approx 10^{-5}$[eV], in this case becomes interesting to analyse the case where it is similar to the typical tunneling rates ($\gamma_{L(R)} \approx 0.01 - 0,1$[eV]), because, when the spontaneous emission rate is slower that tunneling rate, it is practically ignored, which is not desired when we try to analyse optoelectronic behaviours [Thoss and Evers, 2018]. High spontaneous emission rates, as the chosen in Table 4.1, has been measured in experiments of plasmonic nanoantennas [Hoang et al., 2015].

[1] In the case of leads tunneling, this approximation is known as *wide band limit*.

Table 4.1: Nanojunctions parameters. Based on [Harbola et al., 2006, Hoang et al., 2015, Liu and Segal, 2020].

Ground local energy level	ε_g	0.5 eV
Excited local energy level	ε_e	1.5 eV
Hopping rate	t	0.2 eV
Coulomb repulsion energy	U	0.1 eV
Fermi energy	ε_F	ε_g
Room temperature	T_0	290 K
Left tunneling rate	γ_L	0.01 eV
Right tunneling rate	γ_R	0.01 eV
Spontaneous emission rate	γ_{rad}	0.005 eV
Phonon relaxation rate	γ_{ph}	0.01 eV

4.1 Electron transition processes

In Sec. 3.1 is discussed the effect microscopic processes, as induced electron transition processes, in the electron transport. Because the different microscopic processes could be present at the same time, for the analysis of one of them, is considered the simplest conducting array which contains it.

4.1.1 Resonant tunneling

Considering a conducting array with $N = 1$ site and ground local energy level ε_g, connected to the leads, the nanojunction looks like Fig. 4.1(a). Based in parameters in Table 4.1, the nanojunction energy levels are shown in the Fig. 4.1(b), for the left lead (L), the conducting array (C) and the right lead (R) at 1[V] of bias voltage. Arrows represent the transition between the nanojunction energy levels induced by different reservoirs, each one associated to different colors[2]. In this case, the nanojuction performs only electron tunneling with the leads, being the simplest conducting array which contains this microscopic process. The tunneling induces population transference between the conducting array eigenstates $|e_1\rangle = |0_g\rangle$ and $|e_2\rangle = |1_g\rangle$, which represent zero and one electron in the ground local energy level ε_g, respectively.

[2] In the case of tunneling, the color line only shows the movement of a single electron between the nanojunction energy levels, but not the induced transitions between the conducting array eigenstates as in Fig. 3.2.

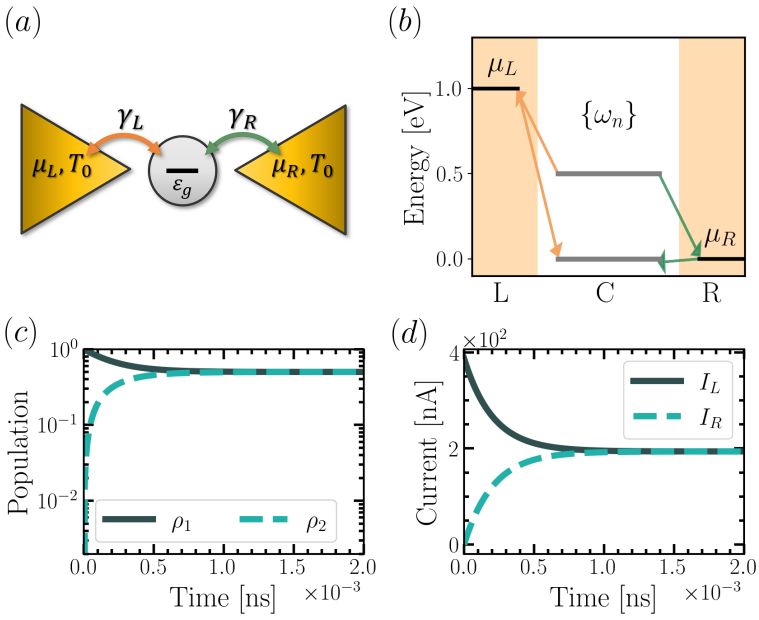

Figure 4.1: For conducting array with $N = 1$ site and ground local energy level ε_g, connected to the leads; (a) nanojunction; (b) nanojunction energy levels for left lead (L), conducting array (C) and right lead (R) at bias voltage of 1[V], where arrows represent electron transference mediated by left lead (yellow), right lead (green), radiation (blue) and phonon (black); population (c) and current (d) evolution from uncharged configuration up to the stationary condition when is applied a bias voltage of $1[V]$. Parameters in Table 4.1.

If initially the conducting array is uncharged, it is, all the population at the conducting array eigenstate $|e_1\rangle$, the population evolution induced by a bias voltage of 1[V] applied constantly is shown in Fig. 4.1(c). The populations evolve up to reach the stationary value $\bar{\rho}_1$ and $\bar{\rho}_2$ after a time of approximately 10^{-3}[ns], which agree with the typical time of the tunneling, $1/(\gamma_L + \gamma_R) \approx 10^{-3}$[ns]. Is expected both populations be equals at the stationary regimen because, based from the rates equations in Eq. (3.8), the stationary populations,

$$\bar{\rho}_1 = \frac{\gamma_L \gamma_R}{\gamma_L + \gamma_R}\left(\frac{\tilde{f}_L^{(2,1)}(V)}{\gamma_R} + \frac{\tilde{f}_R^{(2,1)}(V)}{\gamma_L}\right), \qquad \bar{\rho}_2 = \frac{\gamma_L \gamma_R}{\gamma_L + \gamma_R}\left(\frac{f_L^{(2,1)}(V)}{\gamma_R} + \frac{f_R^{(2,1)}(V)}{\gamma_L}\right), \tag{4.1}$$

at bias voltage V, satifies $\bar{\rho}_1 = \bar{\rho}_2$ when the voltage is swept symmetrically, as in Eq. (3.13), and the tunneling rates, $\gamma_L = \gamma_R$, are equals. At the same time that population evolves, the currents at the interfases evolve, as is shown in Fig. 4.1(d). During the evolution is satisfies $I_L \neq I_R$ because, while populations in the conducting array are evolving, the number of electrons in the conducting array is evolving too, which implies the output and input currents are necessarily different. This explains why currents reach an the stationary value at same time that populations reach an stationary value, verifying the condition $\bar{I}_L = \bar{I}_R$, because the conservation of electron number.

For the nanojunction in Fig. 4.1(a), the computed current-voltage curve is shown in Fig. 4.2(a). The stationary currents satisfy $\bar{I}_L(V) = \bar{I}_R(V)$, because the conservation of electron number, while the expression for the stationary currents at bias voltage V,

$$\bar{I}_L(V) = \bar{I}_R(V) = e\frac{\gamma_L \gamma_R}{\gamma_L + \gamma_R}\left(f_L^{(2,1)}(V) - f_R^{(2,1)}(V)\right), \tag{4.2}$$

computed using the stationary population in Eq. (4.1) and the current definition in Eq. (3.11), explains the symmetric behaviour $\bar{I}_l(V) = -\bar{I}_l(-V)$, when the chemical potentials are swept symmetrically too. As is shown in the current-voltage curve, and according to the stationary current in

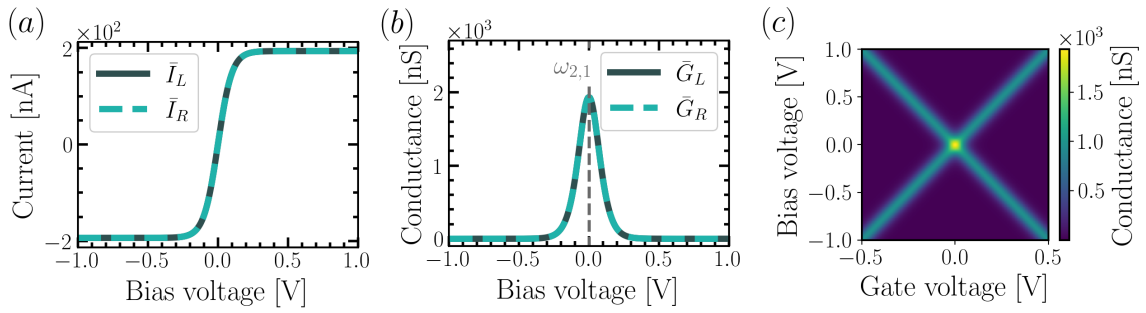

Figure 4.2: For conducting array with $N = 1$ sites and ground local energy level ε_g, connected to the leads; (a) current-voltage curve; (b) conductance-voltage curve, where vertical dotted lines show the electron transition induced by the bias voltage at transition energy $\omega_{n,m}$; (c) conductance-voltage in function of the gate voltage. Parameters in Table 4.1.

Eq. (4.2), the current is zero at zero bias voltage, and different to zero when is applied a non-zero bias voltage. The stationary current increases (decreases) while the voltage increase (decreases), up to reach a saturated current at high bias voltage[3] where the fermion densities, $f_L^{(2,1)}(V)$ and $f_R^{(2,1)}(V)$, becomes constant, and the expression in Eq. (4.2) is reduced to the obtained in [Gurvitz and Prager, 1996, Li et al., 2005]. The sign of the current-voltage curve, means that the electron transport in this nanojuction is such the electrons moves through the conducting array from the highest to the lowest chemical potential, which is intuitive, but having a non-ohmic behaviour.

Is expected a peak of conductance at voltage where the chemical potential of a lead l, μ_l, is the same (resonant) to the energy transition $\omega_{n,m}$, because the fermionic densities $f_l^{(n,m)}$. The conductance-voltage curve shown in Fig. 4.2(b), shows that the conductance of the nanojuction in Fig. 4.1(a) has a peak at zero-bias voltage configuration, because it corresponds where both chemical potentials are resonant with the transition energy $\omega_{2,1} = \omega_g$, represented as a dotted vertical line. It means that the performed second order perturbation theory of the tunneling interaction Hamiltonian, $\hat{\mathcal{H}}_l^{L(R)}$, is included in the nanojunction dynamics as a resonant tunneling process, while higher perturbation theory effects as co-tunneling are not captured. The effect of energy broadening, it is, the widening of conductance peak because the modification of conducting array (self) energies by the coupling with the leads, is not captured because the Born-Markov approximation, unlike with methods based in non-equilibrium Green functions [Pedersen and Wacker, 2005, Esposito and Galperin, 2009].
When the gate voltage appears, the changes of the Fermi energy ε_F tend to split and decrease the conductance peak, as is shown in Fig. 4.2(c), because the chemical potentials become resonant with the transition energy $\omega_{2,1}$ one at time for a non-zero bias voltage configurations.

[3] Defined as the bias voltage range where the current reaches a saturated value.

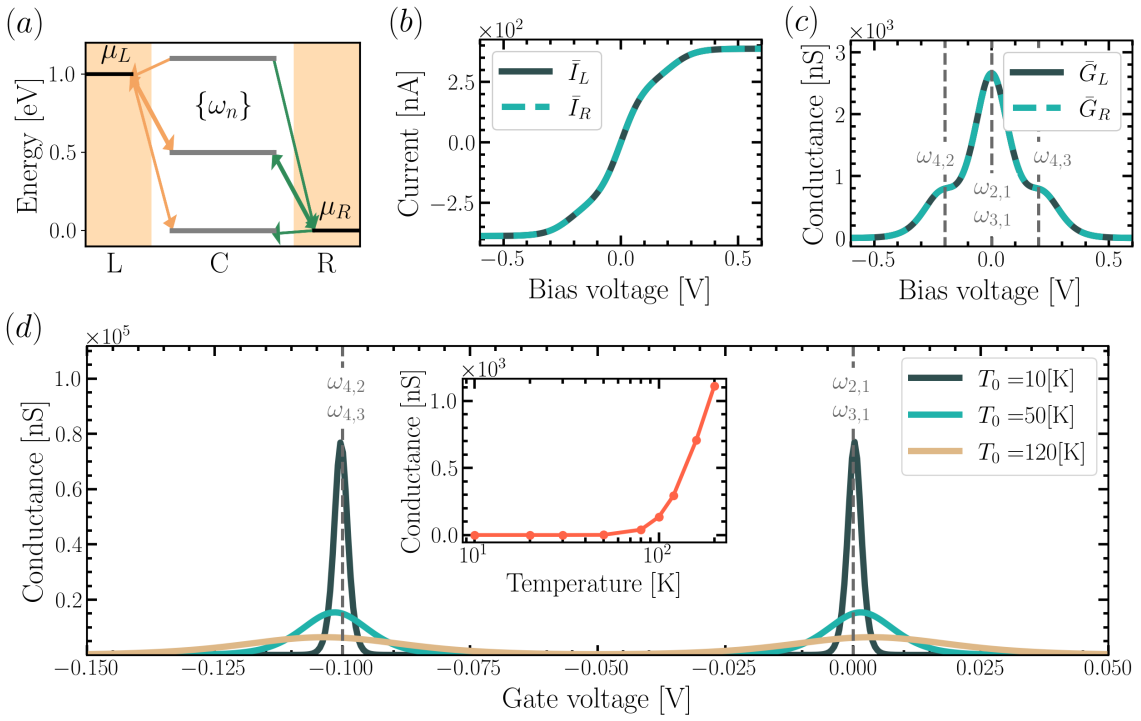

Figure 4.3: For conducting array with $N = 1$ sites and ground local degenerated spin energy level ε_g, connected to the leads; (a) nanojunction energy levels for left lead (L), conducting array (C) and right lead (R), where arrows represent electron transference mediated by left lead (yellow), right lead (green), radiation (blue) and phonon (black) at bias voltage of 1[V]; (b) current-voltage curve; (b) conductance-voltage curve, where vertical dotted lines show the electron transition induced by the voltage at transition energy $\omega_{n,m}$; (d) conductance in function of gate voltage for different environment temperatures, where vertical dotted lines show the electron transition induced by the gate voltage at transition energy $\omega_{n,m}$ (inset: Conductance in function of temperature for magnetic region). Parameters in Table 4.1.

Spin dependent tunneling

The model could taken in to account the electron spin through the index $\sigma = \{\downarrow, \uparrow\}$ for up and down spin, respectively. In the case of conducting array with $N = 1$ sites with a degenerate local spin level ε_g, as the nanojunction looks like Fig. 4.1(a), the nanojunction described by the Hamiltonian,

$$\hat{\mathcal{H}} = \overbrace{\sum_{\sigma} \varepsilon_g \hat{c}^{\dagger}_{1,g,\sigma}\hat{c}_{1,g,\sigma} + \frac{U}{2}\sum_{\sigma\neq\sigma,} \hat{c}^{\dagger}_{1,g,\sigma},\hat{c}_{1,g,\sigma},\hat{c}^{\dagger}_{1,g,\sigma}\hat{c}_{1,g,\sigma}}^{\hat{\mathcal{H}}_C} + \overbrace{\sum_{l,k,\sigma} \omega_k \hat{c}^{\dagger}_{k,l,\sigma}\hat{c}_{k,l,\sigma}}^{\hat{\mathcal{H}}_E} + \underbrace{\sum_{l,k,\sigma} u_i^{(l)}\left(V_k^{(l)}\hat{c}^{\dagger}_{1,g,\sigma}\hat{c}_{l,k,\sigma} + V_k^{(l)*}\hat{c}^{\dagger}_{l,k,\sigma}\hat{c}_{1,g,\sigma}\right)}_{\hat{\mathcal{H}}_I}, \tag{4.3}$$

where $\hat{c}_{1,g,\sigma}$ ($\hat{c}^{\dagger}_{1,g,\sigma}$) annihilates (creates) an electron in the ground level with spin σ at the conducting array site 1 and $\hat{c}_{k,l,\sigma}$ ($\hat{c}^{\dagger}_{k,l,\sigma}$) annihilates (creates) an electron in the mode k from lead l with spin σ, where has been considered the energy of electron in the leads ω_k and the coupling V_k^l spin independent.

Table 4.2: For conducting array with $N = 1$ sites with a degenerated ground local energy level ε_g and ε_e, respectively, and Coulomb repulsion U; conducting array eigenstates $\{|e_n\rangle\}$ with representation in the Fock space and spectrum $\{\omega_n\}$.

Eigenstates	Fock space	Spectrum
$\|e_1\rangle$	$\|0_\uparrow, 0_\downarrow\rangle$	0
$\|e_2\rangle$	$\|0_\uparrow, 1_\downarrow\rangle$	ε_g
$\|e_3\rangle$	$\|1_\uparrow, 0_\downarrow\rangle$	ε_g
$\|e_4\rangle$	$\|1_\uparrow, 1_\downarrow\rangle$	$2\varepsilon_g + U$

The nanojunction energy levels in Fig. 4.3(a) shows that the conducting array performs electron tunneling with the leads. When ground local energy levels is occupied by the electrons in opposite spins, the Coulomb interaction between them appears producing a shift in energy U, as is shown for the eigenstate $|e_4\rangle$ in the Table 4.2.

The current-voltage and conductance-voltage curves are shown in Fig. 4.3(b) and (c), respectively. Compared with the case without spin (see Fig. 4.2), both currents are zero at zero-bias voltage and increases (decreases) at time that bias voltage increases (decreases), but following a different shape and reach different saturated currents, which in the case with spins which is almost double of the saturated current without spin. The last differences are produced because the possibility of having two electrons in the local energy level ε_g, compared with only one electron in the case without spin, as is shown in the conductance-voltage curve, where the spin allows more electron transitions induced by tunneling.

When the gate voltage is applied at zero-bias voltage configuration, the resonant condition of tunneling with the leads is affected. Despite the performed current at zero-bias voltage is zero no matter the gate voltage, the conductance is not necessarily zero, as is shown in Fig. 4.3(d), reaching a conductance peaks at resonant condition, represented by vertical dotted lines. This means that both conductance peaks represent the conducting array is charging process, while the displacement of gate voltage U between them means that Coulomb interaction implies an extra energy for charging the conducting array, as a Coulomb blockade process.
The thermal dependence of conductance peaks comes from the fermion densities, $f_l^{(n,m)}$, which explain why it tends to widen and decreases at time that temperature increases. At the middle of the region between the two conductance peaks, known as the magnetic region[4], the conductance decreases monotonically at time the temperature decrease, as is shown in the inset figure. Therefore, the increasing of conductance at low temperature by Kondo effect is not capture in this model. Is expected that Kondo effect is out the scope of this model [Pedersen and Wacker, 2005], because it arise from the strong correlation between spins at the conducting array and the spins at the leads at low temperature [Kondo, 1964, Andergassen et al., 2010]. For Kondo effect is needed a non-perturbative treatment of the coupling [Esposito and Galperin, 2010], as renormalization group methods [Andergassen et al., 2010].

[4]The region where between conductance peaks where the configuration has total spin $S = 1/2$ and $S = 0$ [Inoshita, 1998].

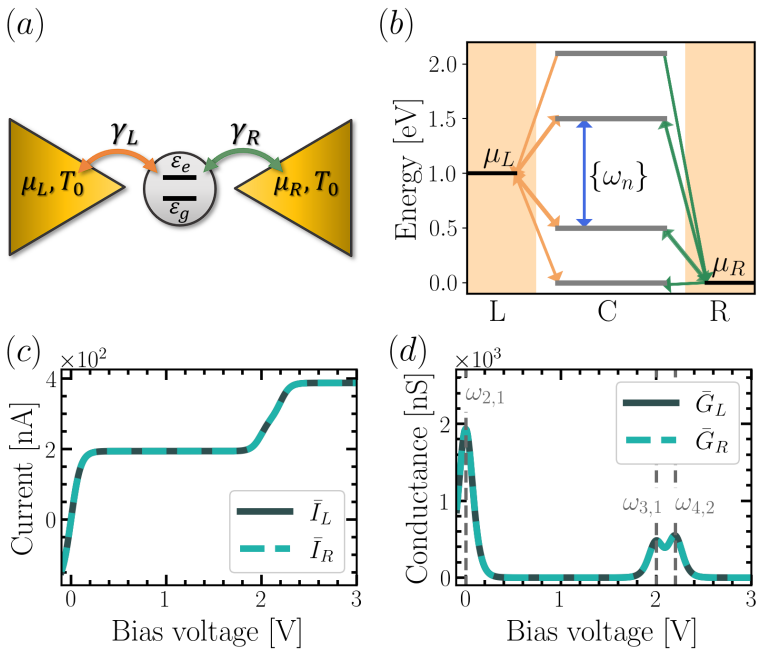

Figure 4.4: For conducting array with $N = 1$ sites, ground and excited local energy level ε_g and ε_e, respectively, and coulomb repulsion U, connected to the leads; (a) nanojunction; (b) nanojunction energy levels for left lead (L), conducting array (C) and right lead (R) at bias voltage of 1[V], where arrows represent electron transference mediated by left lead (yellow), right lead (green), radiation (blue) and phonon (black); (c) current-voltage curve; (d) conductance-voltage curve, where vertical dotted lines show the electron transition induced by the bias voltage at transition energy $\omega_{n,m}$. Parameters in Table 4.1.

4.1.2 Spontaneous emission

For conducting array with $N = 1$ sites, ground and excited local energy level ε_g and ε_e, respectively, and Coulomb repulsion energy U, connected to the leads, the nanojunction looks like the Fig. 4.4(a). The nanojunction energy levels, shown in Fig. 4.4(b), shows that the system performs electron tunneling with the leads and spontaneous emission, being the simplest conducting array which contains the last microscopic process. The spontaneous emission induces population transference between the eigenstate $|e_3\rangle$ to $|e_2\rangle$ (see Table 4.3). The Coulomb interaction appears in the eigenstate $|e_4\rangle$, producing an energy shift U.

The current-voltage curve and conductance-voltage curve are shown in Fig. 4.4(c) and (d), respectively. The stationary current increases at time the chemical potential are resonant with the transition energies, which explain the conductance peaks. For the bias voltage region down the resonance with $\omega_{3,1}$, the electron transport is equal to the case of conducting array with only local ground energy (see Fig. 4.2), because the dynamics in this region is produced only by the eigenstates $|e_1\rangle$ and $|e_2\rangle$, as the last nanojuction. At time that voltage increases, two more conductance

Table 4.3: For conducting array with $N = 1$ sites with ground and excited local energy level ε_g and ε_e, respectively, and Coulomb repulsion U; conducting array eigenstates $\{|e_n\rangle\}$ with representation in the Fock space and spectrum $\{\omega_n\}$.

Eigenstates	Fock space	Spectrum
$\|e_1\rangle$	$\|0_g, 0_e\rangle$	0
$\|e_2\rangle$	$\|1_g, 0_e\rangle$	ε_g
$\|e_3\rangle$	$\|0_g, 1_e\rangle$	ε_e
$\|e_4\rangle$	$\|1_g, 1_e\rangle$	$\varepsilon_g + \varepsilon_e + U$

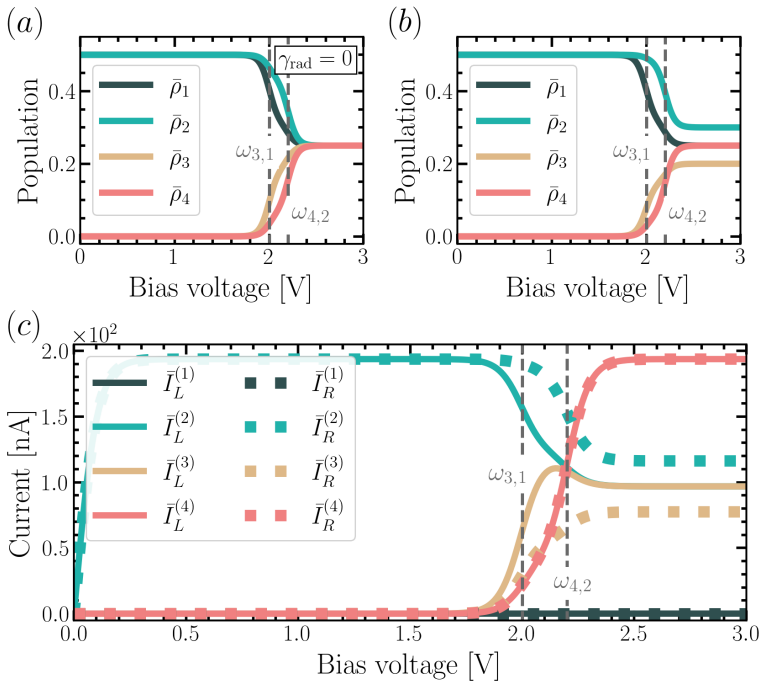

Figure 4.5: For conducting array with $N = 1$ sites, ground and excited local energy level ε_g and ε_e, respectively, and Coulomb repulsion energy U, connected to the leads; stationary populations in function of voltage when (a) the light-matter interaction is off and (b) the light-matter interaction is on; (c) stationary state dependent currents in function of voltage. Parameters in Table 4.1.

peaks produced by the resonance with the transition energies $\omega_{3,1}$ and $\omega_{4,2}$, which implies that current increases, reaching a saturated value after the third conductance peak.

The light-matter interaction incorporates the processes of electron excitation, at rate $\kappa_{\rm rad}^{(3,2)}$, and spontaneous emission, at rate $\tilde{\kappa}_{\rm rad}^{(3,2)}$, in the nanojunction, but, because $\tilde{\kappa}_{\rm rad}^{(3,2)} \gg \kappa_{\rm rad}^{(3,2)}$, the principal effect of light-matter interaction in the nanojunction dynamics is the spontaneous emission. This effect is appreciable in the voltage region where electrons from the leads are tunnelled to the excited levels, it is after $\omega_{3,1}$ and $\omega_{4,2}$. When the light-matter interaction is off (setting $\gamma_{\rm rad} = 0$), in the bias voltage range above the conductance peak at $\omega_{3,1}$, the stationary population $\bar{\rho}_3$ and $\bar{\rho}_4$ increase while $\bar{\rho}_1$ and $\bar{\rho}_2$ decrease, up to reach a value of $\bar{\rho}_1 = \bar{\rho}_2 = \bar{\rho}_3 = \bar{\rho}_4 = 0.25$ at saturated configuration, as is shown in Fig. 4.5(a). When the light-matter interaction is on, shown in Fig. 4.5(b), in the same bias voltage range the behaviour of stationary populations is similar, but the value of the populations affected by spontaneous emission at the saturated configuration is $\bar{\rho}_3 < \bar{\rho}_2$, because the effect of transference of population from $\bar{\rho}_3$ to $\bar{\rho}_2$ by spontaneous emission. Despite the current-voltage curve satisfies $\bar{I}_L = \bar{I}_R$ along the bias voltage, as is shown in Fig. 4.4(c), the stationary state dependent currents does not satisfies necessarily that condition. As is shown in Fig. 4.5(c), the state dependent current in the voltage range above the conductance peak at $\omega_{3,1}$ satisfies $\bar{I}_L^{(2)} < \bar{I}_R^{(2)}$ and $\bar{I}_L^{(3)} > \bar{I}_R^{(3)}$, because, despite the both eigenstates are receiving the same current from the left lead ($\bar{I}_L^{(2)} = \bar{I}_L^{(3)}$), spontaneous emission allows the eigenstate $|e_2\rangle$ transfer to the right also part of the population which comes from eigenstate $|e_3\rangle$. Therefore, is expected that any process, different to the leads tunneling, which induces population transference of an conducting array eigenstate $|e_n\rangle$ will produce that its stationary state dependent current satisfies $\bar{I}_L^{(n)} \neq \bar{I}_R^{(n)}$. This explain why the eigenstates which are not affected by spontaneous emission satisfy $\bar{I}_L^{(1)} = \bar{I}_R^{(1)}$ and $\bar{I}_L^{(4)} = \bar{I}_R^{(4)}$.

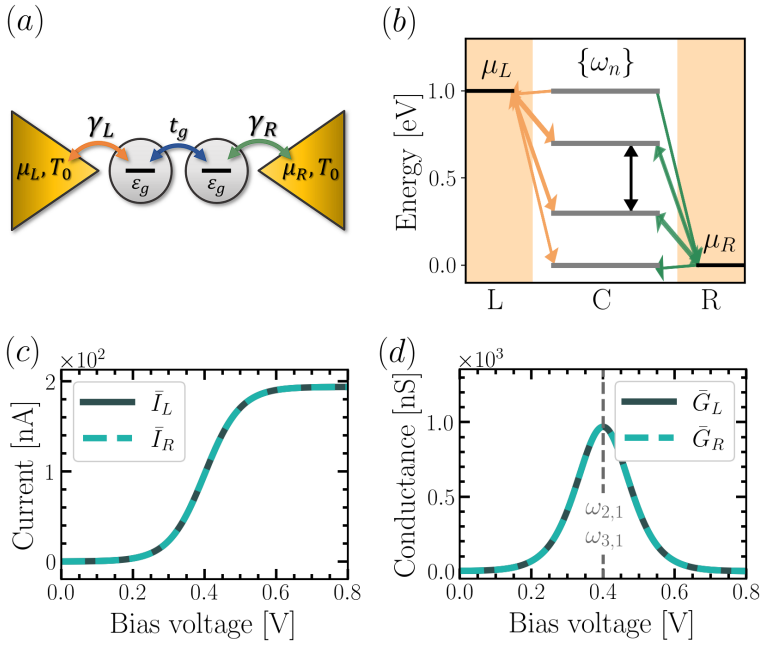

Figure 4.6: For conducting array with $N = 2$ sites, ground local energy level ε_g, and hopping constant t, connected to the leads; (a) nanojunction; (b) nanojunction energy levels for left lead (L), conducting array (C) and right lead (R) at bias voltage of 1[V], where arrows represent electron transference mediated by left lead (yellow), right lead (green), radiation (blue) and phonon (black); (c) current-voltage curve; (d) conductance-voltage curve, where vertical dotted lines show the electron transition induced by the bias voltage at transition energy $\omega_{n,m}$. Parameters in Table 4.1.

4.1.3 Phonon relaxation

Considering a conducting array with $N = 2$ sites, ground local energy levels ε_g and hopping constant $t_g = t$, connected to the leads, the nanojunction looks like the Fig. 4.6(a). The nanojunction energy levels, shown in Fig. 4.6(b), shows that the tight-binding interaction produces an energy splitting $-t$ and t of the delocalized eigenstates $|e_2\rangle$ and $|e_3\rangle$ (see Table 4.4), respectively. The electron-phonon couling is included in the dynamics through a phonon relaxation between the delocalized state, which produce a transference of population between the delocalized eigenstates, being the simplest conducting array which contains the last microscopic process.

The current-voltage and conductance-voltage curve are shown in Fig. 4.6(c) and (d), respectively. The nanojunction begin to performs current when the chemical potentials are resonant with the electron transition $\omega_{2,1}$ and $\omega_{3,1}$, related with the only conductance peak. Is expected conductance peaks when electrons are tunneled to the delocalized eigenstates, because this states

Table 4.4: For conducting array with $N = 2$ sites with ground local energy level ε_g, and hopping constant t; conducting array eigenstates $\{|e_n\rangle\}$ with representation in the Fock space and spectrum $\{\omega_n\}$.

Eigenstates	Fermion Fock space	Spectrum
$\|e_1\rangle$	$\|0_g, 0_e\rangle$	0
$\|e_2\rangle$	$2^{-1/2}\left(\|0_g; 1_g\rangle - \|1_g; 0_g\rangle\right)$	$\varepsilon_g - t$
$\|e_3\rangle$	$2^{-1/2}\left(\|0_g; 1_g\rangle + \|1_g; 0_g\rangle\right)$	$\varepsilon_g + t$
$\|e_4\rangle$	$\|1_g; 1_g\rangle$	$2\varepsilon_g$

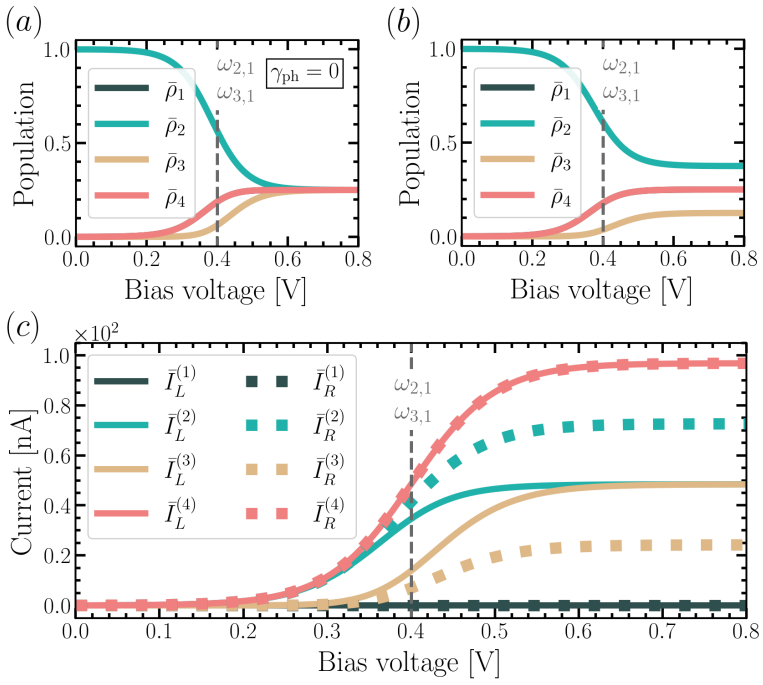

Figure 4.7: For conducting array with $N = 2$ sites, ground local energy level ε_g, and hopping constant t, connected to the leads; stationary populations in function of voltage when (a) the electron-phonon interaction is off and (b) the electron-phonon interaction is on; (c) stationary state dependent currents in function of voltage. Parameters in Table 4.1.

are the only which could do the connection between the leads for electron transport through the conducting array. Therefore is explained why, unlike with the nanojunctions analysed in Sec. 4.1.1 and Sec. 4.1.2, there is not current at zero-bias voltage.

In Fig. 4.7(a) and (b) is shown the stationary populations in function off voltage when the electron-phonon coupling is off ($\gamma_{\rm ph} = 0$) and on, respectively. In the voltage region down the conductance peak, the stationary population is principally accumulates in the eigenstate $|e_1\rangle$, because it receives preferentially electrons from the left lead, but could not transfer to the right lead because is energetically unfavourable. For the voltage region above the conductance peak, when the electron-phonon interaction is off, all the stationary populations reaches the same value at the saturated configuration, while when electron-phonon interaction is on, the stationary populations at the saturated configuration satisfies $\bar{\rho}_2 > \bar{\rho}_3$. The last difference of population is induced by the phonon relaxation because, as was discussed for spontaneous emission in Sec 4.1.2, $\tilde{\kappa}_{\rm ph}^{(3,2)} \gg \kappa_{\rm ph}^{(3,2)}$ and the net effect of electron-phonon coupling is transfer population from $|e_3\rangle$ to $|e_2\rangle$, as a phonon relaxation process.

The state dependent currents in function of voltage, shown in Fig. 4.7(c), shows that for the voltage region above the conductance peak is satisfied $\bar{I}_L^{(2)} \leq \bar{I}_R^{(2)}$ and $\bar{I}_L^{(3)} \geq \bar{I}_R^{(3)}$, while the relations $\bar{I}_L^{(1)} = \bar{I}_R^{(1)}$ and $\bar{I}_L^{(4)} = \bar{I}_R^{(4)}$ are satisfied during all the voltage range. The different between the left and right state dependent current of eigenstates $|e_2\rangle$ and $|e_3\rangle$ happens because the eigenstate $|e_2\rangle$ transfer to the right lead also part of the population which comes from eigenstate $|e_3\rangle$ because the phonon relaxation.

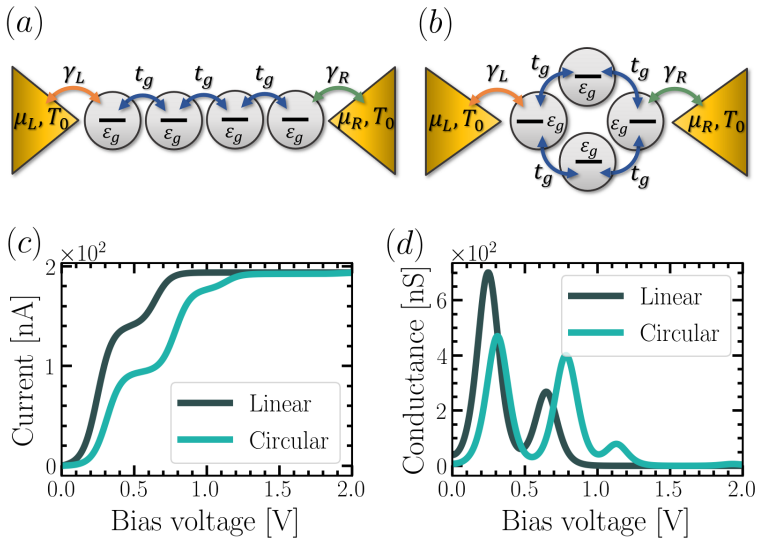

Figure 4.8: For a conducting array with $N = 4$ sites with ground local energy level ε_g, and hopping rates t_g; nanojunction for (a) linear conducting array and (b) circular conducting array; (c) current-voltage curves for linear and circular conducting array; (d) conductance-voltage curves for linear and circular conducting array. Parameters in Table 4.1.

4.2 Geometric array dependence

Considering a conducting array with $N = 4$ sites, ground local energy level ε_g and hopping rate $t_g = t$ in linear and circular geometry, the nanojunctions are shown in Fig. 4.8(a) and (b), respectively. Both nanojunctions performs electron tunneling with the leads and phonon relaxation. As is shown, the differences between both nanojunctions is first the hopping interaction, because in the circular geometry is added hopping interaction between the sites $i = 4$ and $i = 1$, and the sites which connected to the leads, because the right lead coupling with the conducting site $i = 4$ for linear array and with the conducting site $i = 3$ for circular array.

The current-voltage curve for both geometries are shown in Fig. 4.8(c). The different shape of current-voltage curves are explained by the different hopping interactions, which change the conducting array eigenstates and spectrum, and the different sites which interact with the leads, which produce populations transference between different sets of eigenstates at different rates. This reasons also explain why the conductance peaks are localized at different bias-voltages and have different sizes, as is shown in Fig. 4.8(d). Although, the both current looks like a displacement of one respect to the other, reaching a common value of its saturated currents. Compared the saturated current with the obtained by conducting arrays based on ground local levels (see Fig. 4.2(a) and 4.6(c)), all of them reach similar value. Therefore, the value of saturated current is limited principally by considering one local energy level, not by the conducting array geometry.
The stationary state dependent current for linear and circular conducting array at the saturated configuration are shown in Fig. 4.9(a) and (b), respectively. For both geometries, the states dependent contribution looks similar in function of n, which only enumerates the eigenstates from lowest to highest energy. Almost all of the state dependent current are different at the right and left for the set of eigenstates, because the presence of phonon relaxation, as we discussed in Sec. 4.1.3. When the electron-phonon interaction is off ($\gamma_{\rm ph} = 0$), all the state dependent current satisfies $\bar{I}_L^{(n)} = \bar{I}_L^{(n)}$ for all the set of eigenstates as is shown in Fig. 4.9(c) and (d) for linear and circular conducting array, respectively.

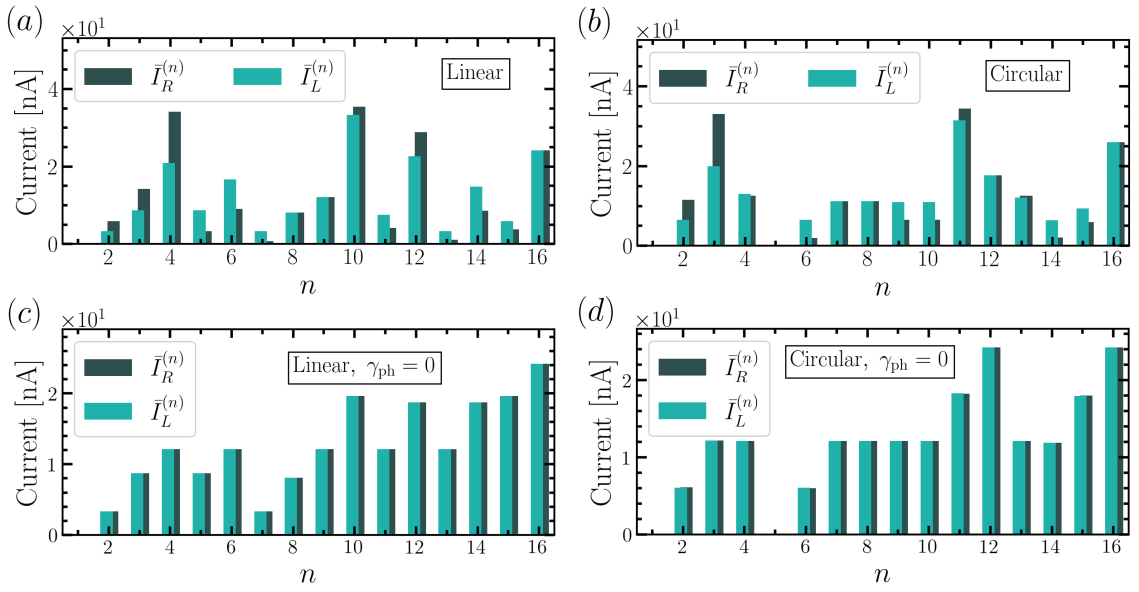

Figure 4.9: For a conducting array with $N = 4$ sites with ground local energy level ε_g, and hopping rates t_g; state dependent current at $2[V]$ bias voltage for (a) linear conducting array and (b) circular conducting array; and when the the electron-phonon interaction is off ($\gamma_{\rm ph} = 0$) for (c) linear conducting array and (d) circular conducting array. Parameters in Table 4.1.

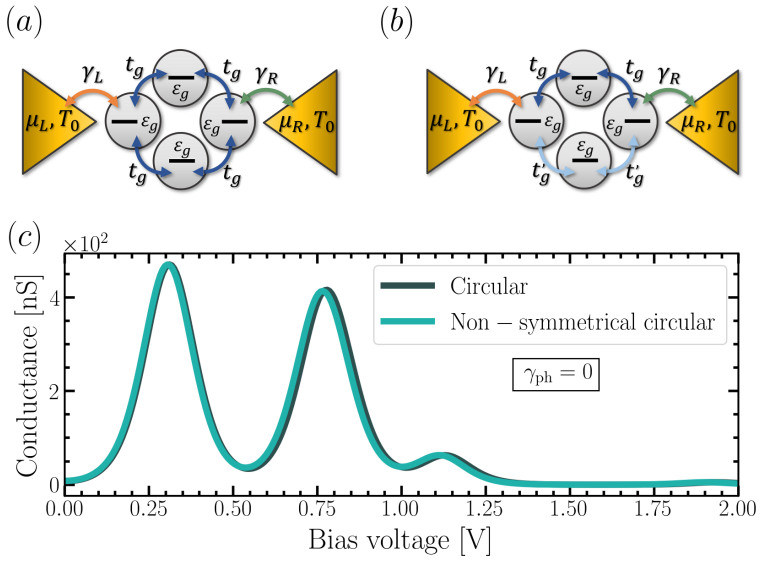

Figure 4.10: For a circular conducting array with $N = 4$ sites with ground local energy level ε_g; (a) nanojunction for symmetric hopping rates t_g ; (b) nanojunction for non-symmetrical hopping rates, with t_g for upper path and t_g' for lower path; (c) current-voltage curves for circular symmetric and non-symmetrical conducting array. Parameters in Table 4.1.

In multiple-path, the wave function, as a complex number, could interferes during the transport, increasing or decreasing the tunneling for constructive and destructive interference, respectively [Taylor et al., 2002]. The process of quantum interference must be maximum when the electron path are indistinguishable, as the upper and lower path in the case of circular array shown in Fig. 4.10(a). Therefore when the path are slightly distinguishable, as a case of non-symmetrical circular conducting array shown in Fig. 4.10(b) where the hopping rate for the upper and lower paths are $t_g = t$ and $t_g' = 0.97t$, respectively, the quantum interference effect must be minimized.

In Fig. 4.10(c) is shown the conductance-voltage curves of circular conducting array symmetric and non-symmetrical, where has been fixed $\gamma_{\rm ph} = 0$ for observing pure tunneling dynamics. The slightly different of their conductance-voltage curves comes from the changes of eigenstates and energies, but is not observed any suppression of currents because the quantum interference, as is expected in this kind of systems [Solomon et al., 2009]. Is expected that quantum interference is not taken into account, because is not the appropriately described in Lindbland quantum master equations[5] [Esposito and Galperin, 2010].

4.3 Incoherent pumping

In the presence of a light source, molecular junctions has demonstrated the phenomena of light-induced current [Lara-Avila et al., 2011, Battacharyya et al., 2011], measured as an enhancement of current because the creation of excited-state molecule, and current-induced light [Qiu et al., 2003, Wu et al., 2008], measured as luminescence because the tunneled excited electrons, which has been also studied theoretically [Galperin and Nitzan, 2005, Galperin and Nitzan, 2006].

In a two-level system, an incoherent pumping source excites electron from the ground to the excited local level incoherently. If this source is applied to the conducting array, at the perturbative regimen the effect on the nanojunction dynamics in taken in to account through a dissipative term,

$$\sum_i W_{\rm Ext}\left(\hat{c}^\dagger_{i,e}\hat{c}_{i,g}\hat{\rho}_C(t)\left(\hat{c}^\dagger_{i,e}\hat{c}_{i,g}\right)^\dagger - \frac{1}{2}\left\{\left(\hat{c}^\dagger_{i,e}\hat{c}_{i,g}\right)^\dagger \hat{c}^\dagger_{i,e}\hat{c}_{i,g}, \hat{\rho}_C(t)\right\}\right), \tag{4.4}$$

in the Lindbland quantum master equation in Eq. (3.4), where $W_{\rm Ext}$ is the incoherent pumping rate, which is modelled as a constant because is assumed with constant spectral density in the range of energy associated to the transition energies. In the secular approximation, the dissipator in Eq. (4.4) becomes,

$$\sum_{n,m} \kappa^{(n,m)}_{\rm Ext}\mathcal{L}_{n,m}\left[\hat{\rho}_C(t)\right], \qquad \kappa^{(n,m)}_{\rm Ext} = W_{\rm Ext}|\left\langle e_n\right|\sum_i \hat{c}^\dagger_{i,e}\hat{c}_{i,g}\left|e_m\right\rangle|^2, \tag{4.5}$$

which means that the incoherent pumping in the conducting array dynamics induces electron transitions between the conducting array eigenstates $|e_m\rangle \rightarrow |e_n\rangle$ with effective transfer rate $\kappa^{(n,m)}_{\rm Ext}$. The effective transfer rates of pumping in Eq. (4.5) follow the same selection rules of eigenstates than excitation by photons, $\kappa^{(n,m)}_{\rm rad}$ (see details in Table B.2).

[5] This was also verified in for the two-site model in Fig. 4.6(a) in a branched distribution, where only one site is coupled to the leads, as the discussed in [Solomon et al., 2009, Esposito and Galperin, 2010].

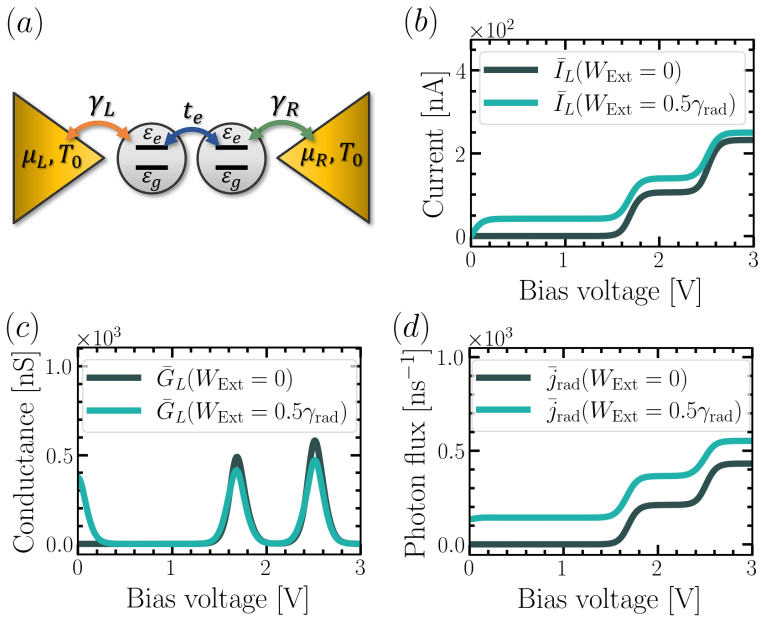

Figure 4.11: For conducting array with $N = 2$ sites with ground and excited local energy level ε_g and ε_e, respectively, Coulomb repulsion energy U and hopping rate t_e, connected to the leads; (a) nanojunction; (b) current-voltage curve in function of incoherent pumping rate; (c) conductance-voltage curve in function of incoherent pumping rate; (d) stationary photon flux in function of bias voltage and pumping rate. Parameters in Table 4.1.

Considering a conducting array with $N = 2$ sites[6], local energy levels ε_g and ε_e, Coulomb repulsion energy U and hopping rate $t_e = t$ only between the excited levels, connected to the leads, the nanojunction looks like the Fig. 4.11(a). The nanojunction performs electron tunneling with the leads, spontaneous emission and phonon relaxation.

The effect of incoherent pumping in the current-voltage curve is shown in the Fig. 4.11(b), where it was considered $W^{\rm Ext}$ up to $0.5\gamma_{\rm rad}$ to be considered as a perturbation and to be valid the two-level approximation in the conducting array sites. It is shown that incoherent pumping produces an offset of current respect to the case without pumping, as a light-induced current process, but conserving similar shape. The incoherent pumping induces the nanojuction performs above non-zero bias voltage, because it transfers electrons from the localized ground eigenstates to the delocalized excited eigenstates, from where the electrons could tunnels preferentially to the lower chemical potentials, which explains the conductance peak at zero bias voltage shown in Fig. 4.11(c). After the first conductance peaks, both current-voltage curves have similar shapes, because this region the current is induced by the electrons tunneled from the leads. With or without incoherent pumping, both currents reach similar saturated value, which is less than other nanojunction based in conducting array with two local energy levels (see Fig. 4.4(c)).

An other interesting observable is the stationary photon flux $\bar{j}_{\rm rad}$ emitted by the conducting array by spontaneous emission. Whit $\hat{\mathcal{N}}_{\rm rad}$ the number operator of photons in the radiation, the photon flux is defined as (see derivation in Appendix C),

$$\bar{j}_{\rm rad} = \frac{d}{dt}\langle \hat{N}_{\rm rad}\rangle = -\sum_{n,m}\left(\kappa_{\rm rad}^{(n,m)}\bar{\rho}_m - \tilde{\kappa}_{\rm rad}^{(n,m)}\bar{\rho}_n\right), \tag{4.6}$$

which quantifies the number of photons per unit of time added to the radiation by the non-equilibrium conducting array dynamics. As is shown in Fig. 4.11(d), the incoherent pumping increases the

[6] It was verified that the effect of incoherent pumping in the case of conducting array with $N = 1$ sites in Fig. 4.4(a) does not affect interestingly the electron transport, because it only tend to apposite the effect of spontaneous emission.

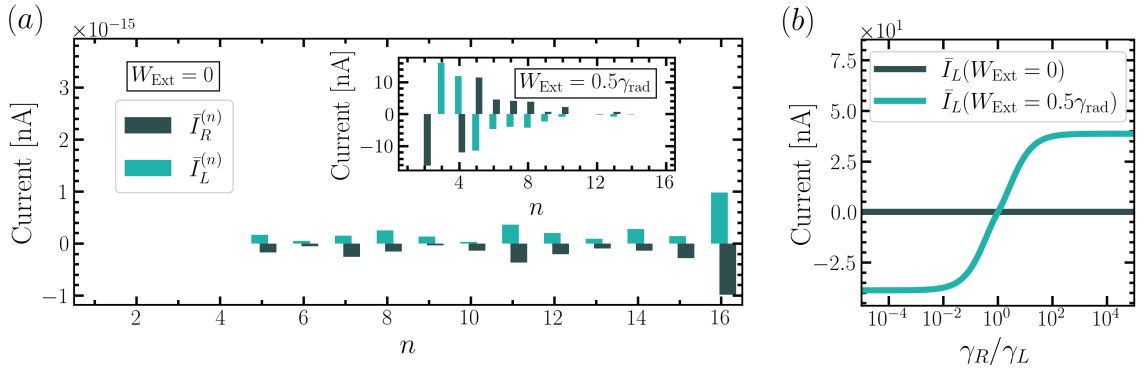

Figure 4.12: For conducting array with $N = 2$ sites, ground and excited local energy level ε_g and ε_e, respectively, Coulomb repulsion energy U and hopping rate t_e, connected to the leads; (a) state dependent currents at 0[V] bias voltage without incoherent pumping rate (inset: case with $W_{\rm Ext} = 0.5\gamma_{\rm rad}$); (b) stationary current at 0[V] bias voltage in function of incoherent pumping rate and tunneling rates. Parameters in Table 4.1.

photon flux respect to the case without it, because the electrons excited by the incoherent pumping could decay by spontaneous emission, emitting a photons in the process. Both curves follow the same behaviour in function of bias voltage because the increasing of photon flux is produced by electrons which previously have been tunnelled from the leads to the excited delocalized eigenstates, as current-induced light process.

When we focus on the zero-bias voltage configuration, despite the stationary currents performed in the nanojunction is zero no matter the incoherent pumping rate (see Fig. 4.11(b)), some stationary state dependent currents, shown in Fig. 4.12(a), have positive and negative values, which satisfy $\bar{I}_L^{(n)} \neq \bar{I}_R^{(n)}$. When the incoherent pumping is off, the stationary state dependent currents are low ($\approx 10^{-15}$[nA]) respect to the saturated current reached by the system ($\approx 10^{2}$[nA]), although not so the case when the incoherent pumping is applied, where there are significant state dependent currents ($\approx 10^{1}$[nA]). Those significant stationary state dependent current at zero-bias voltage when the incoherent pumping is applied are produced because the electrons, which originally are in the localized ground eigenstates, are excited to the delocalized excited eigenstates, which produces that the "free" localized ground eigenstates could receives electrons from the leads while the electrons in the delocalized excited eigenstates could tunnels to the leads. Despite the stationary state dependent currents means that electrons are tunnelled to the leads by the incoherent pumping at zero bias voltage, the stationary current, as the sum of all the state dependent currents in their respective leads, is zero in the both interfases because the tunneling process does not prefer any specific direction when the tunneling rates, γ_L, γ_R, are equals. Nevertheless, when $\gamma_R \neq \gamma_L$[7], is induced an stationary photocurrent to the right direction if $\gamma_R > \gamma_L$ or to the left direction if $\gamma_R < \gamma_L$ at zero bias voltages, as is shown in Fig. 4.12(b). The stationary current at zero bias voltage has a maximum value of approximately 15% of the saturated current performed by the nanojuction. Photocurrents at zero bias voltage when the tunneling rates are different has been predicted before in [Galperin and Nitzan, 2005, Galperin and Nitzan, 2006] for similar system.

[7] The tunneling rates are modifying increasing their values respect to the given in Table 4.1.

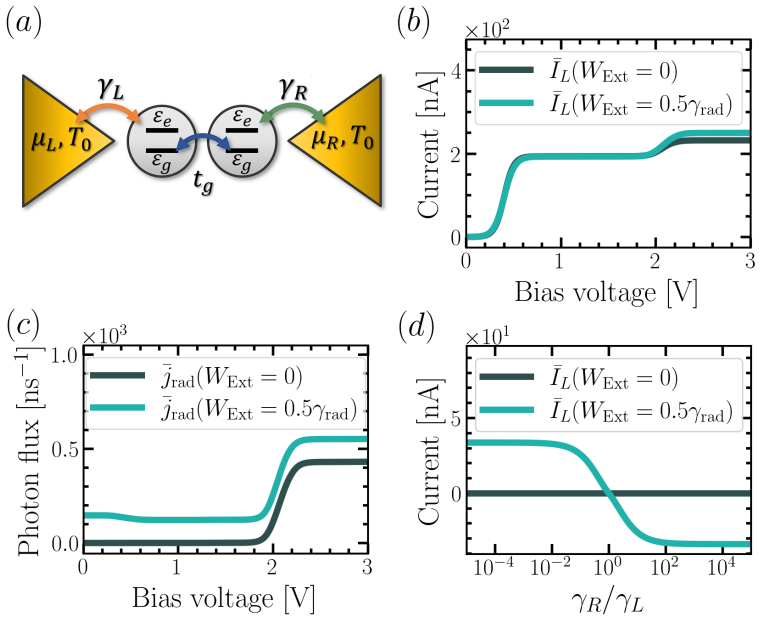

Figure 4.13: For conducting array with $N = 2$ sites, ground and excited local energy level ε_g and ε_e, respectively, Coulomb repulsion energy U and hopping rate t_g, connected to the leads; (a) nanojunction; (b) current-voltage curve in function of incoherent pumping rate; (c) stationary photon flux in function of bias voltage and pumping rate; (d) stationary current at 0[V] bias voltage in function of incoherent pumping rate and tunneling rates. Parameters in Table 4.1.

When the conducting array in Fig. 4.11(a) has hopping constant $t_g = t$ only between the ground levels, the nanojunction looks like the Fig. 4.13(a). The nanojunction also performs electrons tunneling with the leads, spontaneous emission and phonon relaxation, but with different rates and set of eigenstates.

Because the nanojunction is delocalized through the ground eigenstates, is expected the stationary current is not considerably enhanced by the incoherent pumping, as is shown in Fig. 4.13(b), because the spontaneous delocalizes the electrons, meanwhile in the nanojunction in Fig. 4.11(a) the spontaneus emission localizes the electrons, therefore the incoherent pumping do the opposite. Nevertheless, both nanojunctions reach similar saturated currents value.

Because the incoherent pumping is constantly exciting electrons, is expected that the process increase the stationary photon flux respect to the case without it, as we can see in Fig. 4.13(c). The dependence of voltage of photon flux for both cases look similar, because is a current-induced light process.

Because the non-equilibrium dynamic induced by the incoherent pumping at zero bias voltage condition, when tunneling rates are different, is induced an stationary photocurrent to the left direction if $\gamma_R > \gamma_L$ and in the right direction when $\gamma_R < \gamma_L$, with a saturated value of approximately 15%. Compared with the case of hopping through the excited levels (see Fig. 4.12(b)), despite the stationary photocurrent at zero voltage configuration oscillates between similar values, the direction is the opposite. This difference is explained because, while the conducting array delocalized through the excited levels only transfers electron from the delocalized excited eigenstates preferentially to the lead with higher tunneling rates, producing stationary current to the higher tunneling direction, the conducting array delocalized through the ground levels only receives electrons preferentially from the lead with higher tunneling rate to the delocalized ground eigenstates, producing stationary current to the lower tunneling direction.

Conclusions

In this Thesis, we study electron transport in driven nanojunctions. We use the second quantization formalism to describe a nanojunction composed of an array of conducting sites coupled to electronic leads. Conducting sites can represent individual quantum dots or single conjugated molecules. We study the current-voltage dynamics of the nanojunction using the density matrix formalism discussed, solving for the transient and steady-state response of the conducting system by numerically integrating the corresponding Lindblad quantum master equation using Python code developed for this Thesis. Driven-dissipative electron transport systems are common in natural and artificial scenarios. The dissipative operators and rates were defined in agreement previous work in the literature, resulting in analytical expressions for the electron currents through the system that were in agreement with previous work [Gurvitz and Prager, 1996, Li et al., 2005]. The simplicity of our nanojuction model offers simple and intuitive tools for describing electron transport in nanojunctions. The decoupling of populations and coherences in our Lindblad formalism, ensures that the nanojunction dynamics is reduced only to the evolution of population, which could be useful for analyzing electron transport through complex conducting arrays, because the dimensionality of the system dynamics then scales only linearly with the system dimension, while others full quantum master equations scale in principle quadratically with the system dimension.

Under the influence of an external voltage, we studied the dependence of the current-voltage curves on the number of array sites, the geometry of the conducting array, the magnitude of the state-dependent electron tunneling rates, the electron-phonon coupling strength, and the spontaneous emission rate. Additionally, we study the influence of an incoherent light source that pumps energy into the conducting array, on the state-dependent electron current and photon flux through the system. Our results show that resonant electron tunneling explains the positions of the conductance peaks, while spontaneous emission and phonon relaxation processes explain the possible difference between left and right stationary currents for individual system eigenstates. We also show that the electron transport depends on the geometry of the conducting array, for fixed number of sites and local energy levels. However, the value of the saturated current is less dependent on the array geometry, because the dynamics of quantum interferences are not appropriately described with our Lindblad quantum master equation [Esposito and Galperin, 2010]. When the incoherent pumping source is applied on a delocalized electron state within the array, our results agree with the results obtained in [Galperin and Nitzan, 2005, Galperin and Nitzan, 2006], which for a similar system predict light-induced current and current-induced light, and the non-equilibrium dynamics induced with the leads at zero bias voltage can be reflected in stationary photocurrent when the left-right tunneling rates are different. The direction of the induced photocurrent depends

on whether the conducting array has delocalized electrons in the ground or the excited orbital manifolds.

Given our simplified Lindblad master equation approach, several interesting phenomena fall outside of the scope of this Thesis, including polaron effects and other Non-Markovian system-environment interactions that may be relevant in experiments. In the near future, our work can be extended to describe charge and excitation transfer in nanojunction that are strongly coupled to quantized electromagnetic fields, under conditions that favor the formation of hybrid polariton states that are part light and part matter. Experimental [Orgiu et al., 2015, Chikkaraddy et al., 2016] and theoretical [Hagenmüller et al., 2017, Hagenmüller et al., 2018, Schäfer et al., 2019] studies have reported enhanced of currents relative to cavity-free scenario by orders of magnitude. These enhanced currents have been associated with vacuum-induced electron-electron correlations over large distances, and the formation of coherent states which extend over hundreds of molecules. Possible applications of these transport enhancements are currently under intense investigation in the emerging field of molecular polaritons [Herrera and Owrutsky, 2020].

Bibliography

[Andergassen et al., 2010] Andergassen, S., Meden, V., Schoeller, H., Splettstoesser, J., and Wegewijs, M. (2010). Charge transport through single molecules, quantum dots and quantum wires. *Nanotechnology*, 21(27):272001.

[Aviram and Ratner, 1974] Aviram, A. and Ratner, M. A. (1974). Molecular rectifiers. *Chemical physics letters*, 29(2):277–283.

[Ballmann et al., 2012] Ballmann, S., Härtle, R., Coto, P. B., Elbing, M., Mayor, M., Bryce, M. R., Thoss, M., and Weber, H. B. (2012). Experimental evidence for quantum interference and vibrationally induced decoherence in single-molecule junctions. *Physical review letters*, 109(5):056801.

[Battacharyya et al., 2011] Battacharyya, S., Kibel, A., Kodis, G., Liddell, P. A., Gervaldo, M., Gust, D., and Lindsay, S. (2011). Optical modulation of molecular conductance. *Nano letters*, 11(7):2709–2714.

[Breuer et al., 2002] Breuer, H.-P., Petruccione, F., et al. (2002). *The theory of open quantum systems*. Oxford University Press on Demand.

[Bruus and Flensberg, 2004] Bruus, H. and Flensberg, K. (2004). *Many-body quantum theory in condensed matter physics: an introduction*. Oxford university press.

[Burzurí et al., 2014] Burzurí, E., Yamamoto, Y., Warnock, M., Zhong, X., Park, K., Cornia, A., and van der Zant, H. S. (2014). Franck–condon blockade in a single-molecule transistor. *Nano letters*, 14(6):3191–3196.

[Chikkaraddy et al., 2016] Chikkaraddy, R., De Nijs, B., Benz, F., Barrow, S. J., Scherman, O. A., Rosta, E., Demetriadou, A., Fox, P., Hess, O., and Baumberg, J. J. (2016). Single-molecule strong coupling at room temperature in plasmonic nanocavities. *Nature*, 535(7610):127–130.

[Esposito and Galperin, 2009] Esposito, M. and Galperin, M. (2009). Transport in molecular states language: Generalized quantum master equation approach. *Physical Review B*, 79(20):205303.

[Esposito and Galperin, 2010] Esposito, M. and Galperin, M. (2010). Self-consistent quantum master equation approach to molecular transport. *The Journal of Physical Chemistry C*, 114(48):20362–20369.

[Evers et al., 2020] Evers, F., Korytár, R., Tewari, S., and van Ruitenbeek, J. M. (2020). Advances and challenges in single-molecule electron transport. *Reviews of Modern Physics*, 92(3):035001.

[Galperin and Nitzan, 2005] Galperin, M. and Nitzan, A. (2005). Current-induced light emission and light-induced current in molecular-tunneling junctions. *Physical review letters*, 95(20):206802.

[Galperin and Nitzan, 2006] Galperin, M. and Nitzan, A. (2006). Optical properties of current carrying molecular wires. *The Journal of chemical physics*, 124(23):234709.

[Galperin et al., 2006] Galperin, M., Nitzan, A., and Ratner, M. A. (2006). Resonant inelastic tunneling in molecular junctions. *Physical Review B*, 73(4):045314.

[Gauger et al., 2008] Gauger, E. M., Nazir, A., Benjamin, S. C., Stace, T. M., and Lovett, B. W. (2008). Robust adiabatic approach to optical spin entangling in coupled quantum dots. *New Journal of Physics*, 10(7):073016.

[Gehring et al., 2019] Gehring, P., Thijssen, J. M., and van der Zant, H. S. (2019). Single-molecule quantum-transport phenomena in break junctions. *Nature Reviews Physics*, 1(6):381–396.

[Greiner et al., 2012] Greiner, W., Neise, L., and Stöcker, H. (2012). *Thermodynamics and statistical mechanics*. Springer Science & Business Media.

[Gurvitz and Prager, 1996] Gurvitz, S. and Prager, Y. S. (1996). Microscopic derivation of rate equations for quantum transport. *Physical Review B*, 53(23):15932.

[Hagenmüller et al., 2017] Hagenmüller, D., Schachenmayer, J., Schütz, S., Genes, C., and Pupillo, G. (2017). Cavity-enhanced transport of charge. *Physical review letters*, 119(22):223601.

[Hagenmüller et al., 2018] Hagenmüller, D., Schütz, S., Schachenmayer, J., Genes, C., and Pupillo, G. (2018). Cavity-assisted mesoscopic transport of fermions: Coherent and dissipative dynamics. *Physical Review B*, 97(20):205303.

[Harbola et al., 2006] Harbola, U., Esposito, M., and Mukamel, S. (2006). Quantum master equation for electron transport through quantum dots and single molecules. *Physical Review B*, 74(23):235309.

[Herrera and Owrutsky, 2020] Herrera, F. and Owrutsky, J. (2020). Molecular polaritons for controlling chemistry with quantum optics. *The Journal of chemical physics*, 152(10):100902.

[Hoang et al., 2015] Hoang, T. B., Akselrod, G. M., Argyropoulos, C., Huang, J., Smith, D. R., and Mikkelsen, M. H. (2015). Ultrafast spontaneous emission source using plasmonic nanoantennas. *Nature communications*, 6(1):1–7.

[Hubbard, 1963] Hubbard, J. (1963). Electron correlations in narrow energy bands. *Proceedings of the Royal Society of London. Series A. Mathematical and Physical Sciences*, 276(1365):238–257.

[Hubbard, 1967] Hubbard, J. (1967). Electron correlations in narrow energy bands v. a perturbation expansion about the atomic limit. *Proceedings of the Royal Society of London. Series A. Mathematical and Physical Sciences*, 296(1444):82–99.

[Inoshita, 1998] Inoshita, T. (1998). Kondo effect in quantum dots. *Science*, 281(5376):526–527.

[Jeong et al., 2001] Jeong, H., Chang, A. M., and Melloch, M. R. (2001). The kondo effect in an artificial quantum dot molecule. *Science*, 293(5538):2221–2223.

[Kondo, 1964] Kondo, J. (1964). Resistance minimum in dilute magnetic alloys. *Progress of theoretical physics*, 32(1):37–49.

[Kouwenhoven, 1995] Kouwenhoven, L. (1995). Coupled quantum dots as artificial molecules. *Science*, 268(5216):1440–1442.

[Kouwenhoven et al., 1991] Kouwenhoven, L., van der Vaart, N., Johnson, A., Wool, K., and EJ, C. (1991). Harmans, jg williamson, and aam staring. *Z. Phys. B*, 85:367.

[Kouwenhoven et al., 1997] Kouwenhoven, L. P., Marcus, C. M., McEuen, P. L., Tarucha, S., Westervelt, R. M., and Wingreen, N. S. (1997). Electron transport in quantum dots. In *Mesoscopic electron transport*, pages 105–214. Springer.

[Lara-Avila et al., 2011] Lara-Avila, S., Danilov, A. V., Kubatkin, S. E., Broman, S. L., Parker, C. R., and Nielsen, M. B. (2011). Light-triggered conductance switching in single-molecule dihydroazulene/vinylheptafulvene junctions. *The Journal of Physical Chemistry C*, 115(37):18372–18377.

[Leturcq et al., 2009] Leturcq, R., Stampfer, C., Inderbitzin, K., Durrer, L., Hierold, C., Mariani, E., Schultz, M. G., Von Oppen, F., and Ensslin, K. (2009). Franck–condon blockade in suspended carbon nanotube quantum dots. *Nature Physics*, 5(5):327–331.

[Li et al., 2005] Li, X.-Q., Luo, J., Yang, Y.-G., Cui, P., and Yan, Y. (2005). Quantum master-equation approach to quantum transport through mesoscopic systems. *Physical Review B*, 71(20):205304.

[Liu and Segal, 2020] Liu, J. and Segal, D. (2020). Generalized input-output method to quantum transport junctions. ii. applications. *Physical Review B*, 101(15):155407.

[Mahan, 2013] Mahan, G. D. (2013). *Many-particle physics*. Springer Science & Business Media.

[Nitzan, 2006] Nitzan, A. (2006). *Chemical dynamics in condensed phases: relaxation, transfer and reactions in condensed molecular systems*. Oxford university press.

[Nitzan and Ratner, 2003] Nitzan, A. and Ratner, M. A. (2003). Electron transport in molecular wire junctions. *Science*, 300(5624):1384–1389.

[Nolting et al., 2018] Nolting, W. et al. (2018). *Theoretical Physics 8*. Springer.

[Orgiu et al., 2015] Orgiu, E., George, J., Hutchison, J., Devaux, E., Dayen, J., Doudin, B., Stellacci, F., Genet, C., Schachenmayer, J., Genes, C., et al. (2015). Conductivity in organic semiconductors hybridized with the vacuum field. *Nature Materials*, 14(11):1123–1129.

[Park et al., 2002] Park, J., Pasupathy, A. N., Goldsmith, J. I., Chang, C., Yaish, Y., Petta, J. R., Rinkoski, M., Sethna, J. P., Abruña, H. D., McEuen, P. L., et al. (2002). Coulomb blockade and the kondo effect in single-atom transistors. *Nature*, 417(6890):722–725.

[Pedersen and Wacker, 2005] Pedersen, J. N. and Wacker, A. (2005). Tunneling through nanosystems: Combining broadening with many-particle states. *Physical Review B*, 72(19):195330.

[Perrin et al., 2014] Perrin, M. L., Frisenda, R., Koole, M., Seldenthuis, J. S., Gil, J. A. C., Valkenier, H., Hummelen, J. C., Renaud, N., Grozema, F. C., Thijssen, J. M., et al. (2014). Large negative differential conductance in single-molecule break junctions. *Nature nanotechnology*, 9(10):830.

[Qiu et al., 2003] Qiu, X., Nazin, G., and Ho, W. (2003). Vibrationally resolved fluorescence excited with submolecular precision. *Science*, 299(5606):542–546.

[Reed et al., 1997] Reed, M. A., Zhou, C., Muller, C., Burgin, T., and Tour, J. (1997). Conductance of a molecular junction. *Science*, 278(5336):252–254.

[Reimann and Manninen, 2002] Reimann, S. M. and Manninen, M. (2002). Electronic structure of quantum dots. *Reviews of modern physics*, 74(4):1283.

[Schäfer et al., 2019] Schäfer, C., Ruggenthaler, M., Appel, H., and Rubio, A. (2019). Modification of excitation and charge transfer in cavity quantum-electrodynamical chemistry. *Proceedings of the National Academy of Sciences*, 116(11):4883–4892.

[Scheer and Cuevas, 2017] Scheer, E. and Cuevas, J. C. (2017). *Molecular electronics: an introduction to theory and experiment*, volume 15. World Scientific.

[Solomon et al., 2009] Solomon, G. C., Andrews, D. Q., Van Duyne, R. P., and Ratner, M. A. (2009). Electron transport through conjugated molecules: When the π system only tells part of the story. *ChemPhysChem*, 10(1):257–264.

[Sowa et al., 2017] Sowa, J. K., Mol, J. A., Briggs, G. A. D., and Gauger, E. M. (2017). Vibrational effects in charge transport through a molecular double quantum dot. *Physical Review B*, 95(8):085423.

[Sowa et al., 2018] Sowa, J. K., Mol, J. A., Briggs, G. A. D., and Gauger, E. M. (2018). Beyond marcus theory and the landauer-büttiker approach in molecular junctions: A unified framework. *The Journal of chemical physics*, 149(15):154112.

[Tartakovskii, 2012] Tartakovskii, A. (2012). Quantum dots: optics, electron transport and future applications.

[Tarucha et al., 1996] Tarucha, S., Austing, D., Honda, T., Van der Hage, R., and Kouwenhoven, L. P. (1996). Shell filling and spin effects in a few electron quantum dot. *Physical Review Letters*, 77(17):3613.

[Taylor et al., 2002] Taylor, J., Brandbyge, M., and Stokbro, K. (2002). Theory of rectification in tour wires: The role of electrode coupling. *Physical review letters*, 89(13):138301.

[Thoss and Evers, 2018] Thoss, M. and Evers, F. (2018). Perspective: Theory of quantum transport in molecular junctions. *The Journal of chemical physics*, 148(3):030901.

[Timm, 2008] Timm, C. (2008). Tunneling through molecules and quantum dots: Master-equation approaches. *Physical Review B*, 77(19):195416.

[Wu et al., 2008] Wu, S., Nazin, G., and Ho, W. (2008). Intramolecular photon emission from a single molecule in a scanning tunneling microscope. *Physical Review B*, 77(20):205430.

[Xue et al., 1999] Xue, Y., Datta, S., Hong, S., Reifenberger, R., Henderson, J. I., and Kubiak, C. P. (1999). Negative differential resistance in the scanning-tunneling spectroscopy of organic molecules. *Physical Review B*, 59(12):R7852.

[Yoffe, 2001] Yoffe, A. D. (2001). Semiconductor quantum dots and related systems: electronic, optical, luminescence and related properties of low dimensional systems. *Advances in physics*, 50(1):1–208.

Appendix A

Redfield equation

Writing the nanojunction Hamiltonian in Eq. (2.23) as,

$$\hat{\mathcal{H}} = \hat{\mathcal{H}}_0 + \hat{\mathcal{H}}_I, \qquad \hat{\mathcal{H}}_0 = \hat{\mathcal{H}}_C + \hat{\mathcal{H}}_E, \tag{A.1}$$

any operator $\hat{\mathcal{A}}$ in the Schrödinger picture could be written in interaction picture $\hat{\mathcal{A}}_{\text{'}}(t)$ respect to $\hat{\mathcal{H}}_I$, and vice versa, following the transformations,

$$\hat{\mathcal{A}}_{\text{'}}(t) = \hat{U}\hat{\mathcal{A}}\hat{U}^{\dagger}, \qquad \hat{A} = \hat{U}^{\dagger}\hat{A}_{\text{'}}(t)\hat{U}, \tag{A.2}$$

where the operator $\hat{U} = \exp\left(i\hat{\mathcal{H}}_0 t\right)$ acts as a unitary transformation.

Writing the nanojunction density operator $\hat{\rho}$ in the interaction picture according the Eq. (A.2), the Liouville equation (see Eq. (2.9)) becomes,

$$\frac{d}{dt}\hat{\rho}_{\text{'}}(t) = -i\left[\hat{\mathcal{H}}_{I_{\text{'}}}(t), \hat{\rho}_{\text{'}}(t)\right], \tag{A.3}$$

where $\hat{\mathcal{H}}_{I_{\text{'}}}(t)$ is the Hamiltonian interaction in the interaction picture. Applying direct integration from t_0 to t in Eq.(A.3), is obtained,

$$\hat{\rho}_{\text{'}}(t) = \hat{\rho}_{\text{'}}(t_0) - i\int_{t_0}^{t} dt_{\text{'}}\left[\hat{\mathcal{H}}_{I_{\text{'}}}(t_{\text{'}}), \hat{\rho}_{\text{'}}(t_{\text{'}})\right], \tag{A.4}$$

which, inserted in Eq. (A.3), gives,

$$\frac{d}{dt}\hat{\rho}_{\text{'}}(t) = -\frac{i}{\hbar}\left[\hat{\mathcal{H}}_{I_{\text{'}}}(t), \hat{\rho}_{\text{'}}(t_0)\right] - \int_{t_0}^{t} dt_{\text{'}}\left[\hat{\mathcal{H}}_{I_{\text{'}}}(t), \left[\hat{\mathcal{H}}_{I_{\text{'}}}(t_{\text{'}}), \hat{\rho}_{\text{'}}(t_{\text{'}})\right]\right], \tag{A.5}$$

which add a term in second power of $\hat{\mathcal{H}}_{I_{\text{'}}}$.

Writing the density operator as in Eq. (3.1), the conducting array dynamics from the Eq. (A.5) is,

$$\frac{d}{dt}\hat{\rho}_C^{\cdot}(t) = -\int_{t_0}^{t} dt^{\cdot} \mathrm{Tr}_E \left[\hat{\mathcal{H}}_I^{\cdot}(t), \left[\hat{\mathcal{H}}_I^{\cdot}(t^{\cdot}), \hat{\rho}_C^{\cdot}(t^{\cdot}) \otimes \hat{\rho}_E\right]\right], \tag{A.6}$$

where is verified,

$$\mathrm{Tr}_E[\hat{\mathcal{H}}_I^{\cdot}(t), \hat{\rho}_C^{\cdot}(t_0) \otimes \hat{\rho}_E] = 0, \tag{A.7}$$

because the form of $\hat{\mathcal{H}}_I$ (see Eq. (2.55)) and $\hat{\rho}_E$ (see Eq. (3.2)).
Considering Markov approximation ($\hat{\rho}_C^{\cdot}(t^{\cdot}) \approx \hat{\rho}_C^{\cdot}(t)$) and the transformation $t^{\cdot} = t - \tau$, the Eq. (A.6) becomes,

$$\frac{d}{dt}\hat{\rho}_C^{\cdot}(t) = -\int_{0}^{\infty} d\tau \mathrm{Tr}_E \left[\hat{\mathcal{H}}_I^{\cdot}(t), \left[\hat{\mathcal{H}}_I^{\cdot}(t-\tau), \hat{\rho}_C^{\cdot}(t) \otimes \hat{\rho}_E\right]\right], \tag{A.8}$$

where the integral was extended to $t - t_0 \to \infty$ because the low correlation decay time.
Writing the conducting array dynamics in the Schrödinger picture, is obtained the Redfield equation shown in Eq. (3.3).

Appendix B

Lindbland quantum master equation

Considering a conducting array Hamiltonian $\hat{\mathcal{H}}_C$ in terms of the eigenstates as Eq. (2.39), the reservoir Hamiltonians from Eq. (3.2),

$$\hat{\mathcal{H}}_\lambda = \sum_x \omega_x \hat{u}^\dagger_{\lambda,x} \hat{u}_{\lambda,x}, \tag{B.1}$$

in terms of annihilation and creation operators, $\hat{u}_{\lambda,x}$ and $\hat{u}^\dagger_{\lambda,x}$, respectively, of particles in the reservoir λ at the mode x with energy ω_x, and the interaction Hamiltonian $\hat{\mathcal{H}}_I$ from Eq. (2.55) in separable form as,

$$\hat{\mathcal{H}}_I = \sum_\lambda \left(\hat{\mathcal{S}}_\lambda \hat{\mathcal{R}}_\lambda + \hat{\mathcal{S}}^\dagger_\lambda \hat{\mathcal{R}}^\dagger_\lambda \right), \quad \hat{\mathcal{H}}_I(t) = \sum_\lambda \left(\hat{\mathcal{S}}_\lambda(t) \hat{\mathcal{R}}_\lambda(t) + \hat{\mathcal{S}}^\dagger_\lambda(t) \hat{\mathcal{R}}^\dagger_\lambda(t) \right), \tag{B.2}$$

in the Schrödinger and interaction picture (see Eq. (A.2)), respectively, where the conducting array part $\hat{S}_\lambda$ (see Table B.1) could be written in terms of conducting array eigenstates as,

$$\hat{\mathcal{S}}_\lambda = \sum_{n,m} \mathcal{S}^{(n,m)}_\lambda \hat{L}_{n,m}, \quad \hat{S}_\lambda(t) = \sum_{n,m} \mathcal{S}^{(n,m)}_\lambda \exp\left(i\omega_{n,m} t\right) \hat{L}_{n,m}, \tag{B.3}$$

whit $\mathcal{S}^{(n,m)}_\lambda = \langle e_n | \hat{\mathcal{S}}_\lambda | e_m \rangle$, $\hat{L}_{n,m} = |e_n\rangle \langle e_m|$ and $\omega_{n,m} = \omega_n - \omega_m$, while the reservoir part (see Table B.1) has a form,

$$\hat{\mathcal{R}}_\lambda = \sum_x V^{(\lambda)}_x \hat{u}_{\lambda,x}, \quad \hat{\mathcal{R}}_\lambda(t) = \sum_x V^{(\lambda)}_x \exp\left(-i\omega_x t\right) \hat{u}_{\lambda,x}, \tag{B.4}$$

whit V^λ_x the coupling constants of mode x of the reservoir λ .

Table B.1: Conducting array part, $\hat{\mathcal{S}}_\lambda$, and reservoir part, $\hat{\mathcal{R}}_\lambda$, from the interaction Hamiltonian in Eq. (2.55).

Reservoir (λ)	Conducting array part ($\hat{\mathcal{S}}_\lambda$)	Reservoir part ($\hat{\mathcal{R}}_\lambda$)
Left lead	$\sum_{i,\alpha} u_i^{(L)} \hat{c}_{i,\alpha}^\dagger$	$\sum_k V_k^{(L)} \hat{c}_{L,k}$
Right lead	$\sum_{i,\alpha} u_i^{(R)} \hat{c}_{i,\alpha}^\dagger$	$\sum_k V_k^{(R)} \hat{c}_{R,k}$
Radiation	$\sum_{i,\alpha>\alpha'} u_i^{(\mathrm{rad})} \hat{c}_{i,\alpha}^\dagger \hat{c}_{i,\alpha'}$	$\sum_p V_p^{(\mathrm{rad})} \hat{a}_{\mathrm{rad},p}$
Phonon	$\sum_{i,\alpha} u_i^{(\mathrm{ph})} \hat{c}_{i,\alpha}^\dagger \hat{c}_{i,\alpha}$	$\sum_q V_q^{(\mathrm{rad})} \hat{a}_{\mathrm{ph},q}$

Whit the environment density operator $\hat{\rho}_E$ as Eq. (3.2), any reservoir λ is described as a thermal equilibrium density operators (see Sec. 2.1.4), according to,

$$\hat{\rho}_\lambda = \begin{cases} \frac{\exp\left(-\beta_0(\hat{\mathcal{H}}_\lambda - \mu_\lambda \hat{\mathcal{N}}_\lambda)\right)}{\mathcal{Z}}, \quad \mathcal{Z} = \prod_x \left(1 + \exp\left(-\beta_0(\omega_x - \mu_\lambda)\right)\right)^{-1}, & \text{Fermions} \\ \\ \frac{\exp\left(-\beta_0 \hat{\mathcal{H}}_\lambda\right)}{Z}, \quad Z = \prod_x \left(1 - \exp\left(-\beta_0 \omega_x\right)\right)^{-1}, & \text{Bosons} \end{cases} \tag{B.5}$$

for fermion and boson reservoirs, where,

$$\hat{\mathcal{N}}_\lambda = \sum_x \hat{u}_{\lambda,x}^\dagger \hat{u}_{\lambda,x}, \tag{B.6}$$

is the number operator of particles in the reservoir λ.

The term,

$$I = \mathrm{Tr}_E \left[\hat{\mathcal{H}}_I, \left[\hat{\mathcal{H}}_I(-\tau), \hat{\rho}_C \otimes \hat{\rho}_E\right]\right] \tag{B.7}$$

from the Redfield equation (see Eq. (3.3)), based in the interaction Hamiltonian in Eq. (B.2), becomes,

$$\begin{aligned} I = \sum_\lambda \Big[&\left(\hat{\mathcal{S}}_\lambda^\dagger \hat{\mathcal{S}}_\lambda(-\tau)\hat{\rho}_C - \hat{S}_\lambda(-\tau)\hat{\rho}_C \hat{\mathcal{S}}_\lambda^\dagger\right) C_\lambda(\tau) + \left(\hat{\rho}_C \hat{\mathcal{S}}_\lambda^\dagger(-\tau)\hat{\mathcal{S}}_\lambda - \hat{\mathcal{S}}_\lambda \hat{\rho}_C \hat{\mathcal{S}}_\lambda^\dagger(-\tau)\right) C_\lambda(-\tau) \\ &+ \left(\hat{\mathcal{S}}_\lambda \hat{\mathcal{S}}_\lambda^\dagger(-\tau)\hat{\rho}_C - \hat{\mathcal{S}}_\lambda^\dagger(-\tau)\hat{\rho}_C \hat{\mathcal{S}}_\lambda\right) \tilde{C}_\lambda(\tau) + \left(\hat{\rho}_C \hat{\mathcal{S}}_\lambda(-\tau)\hat{\mathcal{S}}_\lambda^\dagger - \hat{\mathcal{S}}_\lambda^\dagger \hat{\rho}_C \hat{\mathcal{S}}_\lambda(-\tau)\right) \tilde{C}_\lambda(-\tau)\Big], \end{aligned} \tag{B.8}$$

where has been defined,

$$\begin{aligned} C_\lambda(\tau) &= \langle \hat{\mathcal{R}}_\lambda^\dagger \hat{\mathcal{R}}_\lambda(-\tau)\rangle = \sum_x |V_x^{(\lambda)}|^2 \exp(i\omega_x \tau) \mathrm{Tr}_\lambda \left[\hat{\rho}_\lambda \hat{u}_{\lambda,x}^\dagger \hat{u}_{\lambda,x}\right], \\ \tilde{C}_\lambda(\tau) &= \langle \hat{\mathcal{R}}_\lambda \hat{\mathcal{R}}_\lambda^\dagger(-\tau)\rangle = \sum_x |V_x^{(\lambda)}|^2 \exp(-i\omega_x \tau) \mathrm{Tr}_\lambda \left[\hat{\rho}_\lambda \hat{u}_{\lambda,x} \hat{u}_{\lambda,x}^\dagger\right], \end{aligned} \tag{B.9}$$

the reservoir correlation functions.

Whit the thermal equilibrium density operators in Eq. (B.5), the correlations are reduced to,

$$
\begin{aligned}
C_\lambda(\tau) = \langle \hat{\mathcal{R}}_\lambda^\dagger \hat{\mathcal{R}}_\lambda(-\tau)\rangle &= \begin{cases} \sum_x |V_x^{(\lambda)}|^2 f_\lambda^{(x)} \exp\left(i\omega_x\tau\right), & \text{Fermions} \\ \\ \sum_x |V_x^{(\lambda)}|^2 n_\lambda^{(x)} \exp\left(i\omega_x\tau\right), & \text{Bosons} \end{cases} \\
\tilde{C}_\lambda(\tau) = \langle \hat{\mathcal{R}}_\lambda \hat{\mathcal{R}}_\lambda^\dagger(-\tau)\rangle &= \begin{cases} \sum_x |V_x^{(\lambda)}|^2 \tilde{f}_\lambda^{(x)} \exp\left(-i\omega_x\tau\right), & \text{Fermions} \\ \\ \sum_x |V_x^{(\lambda)}|^2 \tilde{n}_\lambda^{(x)} \exp\left(-i\omega_x\tau\right), & \text{Bosons} \end{cases}
\end{aligned}
\tag{B.10}
$$

where has been defined,

$$
\begin{aligned}
f_\lambda(\omega_x) \equiv f_\lambda^{(x)} = 1 - \tilde{f}_\lambda^{(x)} &= \left(\exp\left(\beta_0(\omega_x - \mu_\lambda)\right) + 1\right)^{-1}, \\
n_\lambda(\omega_x) \equiv n_\lambda^{(x)} = \tilde{n}_\lambda^{(x)} - 1 &= \left(\exp\left(\beta_0\omega_x\right) - 1\right)^{-1},
\end{aligned}
\tag{B.11}
$$

the fermion and boson density, respectively, at energy ω_x.

Whit conducting array part in Eq. (B.3) and correlations in Eq. (B.10), the term I in Eq. (B.8) becomes,

$$
\begin{aligned}
I = \sum_\lambda \sum_{n,m,i,j} \mathcal{S}_\lambda^{(n,m)} \mathcal{S}_\lambda^{(i,j)*} \Big[& \left(\hat{L}_{i,j}^\dagger \hat{L}_{n,m} \hat{\rho}_C - \hat{L}_{n,m} \hat{\rho}_C \hat{L}_{i,j}^\dagger\right) C_\lambda(\tau) \exp\left(-i\omega_{n,m}\tau\right) \\
& + \left(\hat{\rho}_C \hat{L}_{i,j}^\dagger \hat{L}_{n,m} - \hat{L}_{n,m} \hat{\rho}_C \hat{L}_{i,j}^\dagger\right) C_\lambda(-\tau) \exp\left(i\omega_{i,j}\tau\right) \\
& + \left(\hat{L}_{n,m} \hat{L}_{i,j}^\dagger \hat{\rho}_C - \hat{L}_{i,j}^\dagger \hat{\rho}_C \hat{L}_{n,m}\right) \tilde{C}_\lambda(\tau) \exp\left(i\omega_{i,j}\tau\right) \\
& + \left(\hat{\rho}_C \hat{L}_{n,m} \hat{L}_{i,j}^\dagger - \hat{L}_{i,j}^\dagger \hat{\rho}_C \hat{L}_{n,m}\right) \tilde{C}_\lambda(-\tau) \exp\left(-i\omega_{n,m}\tau\right) \Big],
\end{aligned}
\tag{B.12}
$$

which, in the interaction picture, has a form,

$$
\begin{aligned}
I' = \sum_\lambda \sum_{n,m,i,j} \mathcal{S}_\lambda^{(n,m)} \mathcal{S}_\lambda^{(i,j)*} \exp\left(i(\omega_{n,m} - \omega_{i,j})t\right) \Big[& \left(\hat{L}_{i,j}^\dagger \hat{L}_{n,m} \hat{\rho}_C' - \hat{L}_{n,m} \hat{\rho}_C' \hat{L}_{i,j}^\dagger\right) C_\lambda(\tau) \exp\left(-i\omega_{n,m}\tau\right) \\
& + \left(\hat{\rho}_C' \hat{L}_{i,j}^\dagger \hat{L}_{n,m} - \hat{L}_{n,m} \hat{\rho}_C' \hat{L}_{i,j}^\dagger\right) C_\lambda(-\tau) \exp\left(i\omega_{i,j}\tau\right) \\
& + \left(\hat{L}_{n,m} \hat{L}_{i,j}^\dagger \hat{\rho}_C' - \hat{L}_{i,j}^\dagger \hat{\rho}_C' \hat{L}_{n,m}\right) \tilde{C}_\lambda(\tau) \exp\left(i\omega_{i,j}\tau\right) \\
& + \left(\hat{\rho}_C' \hat{L}_{n,m} \hat{L}_{i,j}^\dagger - \hat{L}_{i,j}^\dagger \hat{\rho}_C' \hat{L}_{n,m}\right) \tilde{C}_\lambda(-\tau) \exp\left(-i\omega_{n,m}\tau\right) \Big],
\end{aligned}
\tag{B.13}
$$

which oscillates in function of time with frequency $\omega_{n,m} - \omega_{i,j}$, at least $n = i$ and $m = j$ as secular approximation.

The reconstruction of the Redfield equation needs to integrate the correlation functions, which,

Table B.2: Effective transfer rates, $\kappa_\lambda^{(n,m)}$ and $\tilde{\kappa}_\lambda^{(n,m)}$, for reservoir λ.

λ	$\kappa_\lambda^{(n,m)}$	$\tilde{\kappa}_\lambda^{(n,m)}$
L	$\gamma_L^{(n,m)} f_L^{(n,m)} \lvert \langle e_n \rvert \sum_{i,\alpha} u_i^{(L)}\ \hat{c}_{i,\alpha}^\dagger \lvert e_m \rangle \rvert^2$	$\gamma_L^{(n,m)} \tilde{f}_L^{(n,m)} \lvert \langle e_n \rvert \sum_{i,\alpha} u_i^{(L)}\ \hat{c}_{i,\alpha}^\dagger \lvert e_m \rangle \rvert^2$
R	$\gamma_R^{(n,m)} f_R^{(n,m)} \lvert \langle e_n \rvert \sum_{i,\alpha} u_i^{(R)}\ \hat{c}_{i,\alpha}^\dagger \lvert e_m \rangle \rvert^2$	$\gamma_R^{(n,m)} \tilde{f}_R^{(n,m)} \lvert \langle e_n \rvert \sum_{i,\alpha} u_i^{(R)}\ \hat{c}_{i,\alpha}^\dagger \lvert e_m \rangle \rvert^2$
rad	$\gamma_{\text{rad}}^{(n,m)} n_{\text{rad}}^{(n,m)} \lvert \langle e_n \rvert \sum_{i,\alpha>\alpha'} u_i^{(\text{rad})}\ \hat{c}_{i,\alpha}^\dagger \hat{c}_{i,\alpha'} \lvert e_m \rangle \rvert^2$	$\gamma_{\text{rad}}^{(n,m)} \tilde{n}_{\text{rad}}^{(n,m)} \lvert \langle e_n \rvert \sum_{i,\alpha>\alpha'} u_i^{(\text{rad})}\ \hat{c}_{i,\alpha}^\dagger \hat{c}_{i,\alpha'} \lvert e_m \rangle \rvert^2$
ph	$\gamma_{\text{ph}}^{(n,m)} n_{\text{ph}}^{(n,m)} \lvert \langle e_n \rvert \sum_{i,\alpha} u_i^{(\text{ph})}\ \hat{c}_{i,\alpha}^\dagger \hat{c}_{i,\alpha} \lvert e_m \rangle \rvert^2$	$\gamma_{\text{ph}}^{(n,m)} \tilde{n}_{\text{ph}}^{(n,m)} \lvert \langle e_n \rvert \sum_{i,\alpha} u_i^{(\text{ph})}\ \hat{c}_{i,\alpha}^\dagger \hat{c}_{i,\alpha} \lvert e_m \rangle \rvert^2$

through the Cauchy principal value theorem, are,

$$\begin{aligned}
\int_0^\infty d\tau C_\lambda(\pm\tau) \exp\left(\mp i\omega_{n,m}\tau\right) &= \begin{cases} \frac{1}{2}\gamma_\lambda^{(n,m)} f_\lambda^{(n,m)}, & \text{Fermions} \\ \\ \frac{1}{2}\gamma_\lambda^{(n,m)} n_\lambda^{(n,m)}, & \text{Bosons} \end{cases} \\
\int_0^\infty d\tau \tilde{C}_\lambda(\pm\tau) \exp\left(\pm i\omega_{n,m}\tau\right) &= \begin{cases} \frac{1}{2}\gamma_\lambda^{(n,m)} \tilde{f}_\lambda^{(n,m)}, & \text{Fermions} \\ \\ \frac{1}{2}\gamma_\lambda^{(n,m)} \tilde{n}_\lambda^{(n,m)}, & \text{Bosons} \end{cases}
\end{aligned} \tag{B.14}$$

where has been defined the spectral density,

$$\gamma_\lambda(\omega) = \pi \sum_x |V_x^{(\lambda)}|^2 \delta(\omega - \omega_x), \tag{B.15}$$

such $\gamma_\lambda^{(n,m)} = \gamma_\lambda(\omega_{n,m})$ is the spectral density at transition energy $\omega_{n,m}$, and the typical Lamp shift has been ignored.

Writing I, from Eq. (B.12), in the secular approximation and the integrated correlation functions as Eq. (B.14), the Redfield equation becomes in the Lindbland quantum master equation shown in Eq. (3.4), where the *effective transfer rates*, $\kappa_\lambda^{(n,m)}$ and $\tilde{\kappa}_\lambda^{(n,m)}$, are shown in the Table B.2.

Appendix C

Reservoir particles evolution

The evolution of the nanojunction density operator $\hat{\rho}$ in the Schrödinger picture and Markov approximation, from the Eq. (A.5), is given by,

$$\frac{d}{dt}\hat{\rho} = -i\left[\hat{\mathcal{H}}_C, \hat{\rho}\right] - i\,\hat{U}^\dagger\left[\hat{\mathcal{H}}_I(t), \hat{\rho}(t_0)\right]\hat{U} - \int_0^\infty d\tau\left[\hat{\mathcal{H}}_I\left[\hat{\mathcal{H}}_I(-\tau), \hat{\rho}\right]\right], \tag{C.1}$$

where $\hat{U}$ was defined in Eq. (A.2). With $\hat{\mathcal{N}}_\lambda$ the number operator of particle in the reservoir λ (see Eq. (B.6)), based in the Eq. (C.1), the variation of particles is,

$$\frac{d}{dt}\langle\hat{\mathcal{N}}_\lambda\rangle = -\mathrm{Tr}\left[\hat{\mathcal{N}}_\lambda\int_0^\infty d\tau\left[\hat{\mathcal{H}}_I, \left[\hat{\mathcal{H}}_I(-\tau), \hat{\rho}_C\otimes\rho_E\right]\right]\right], \tag{C.2}$$

where Tr performs the trace over the conducting array and the environment.
Whit the interaction Hamiltonian $\hat{\mathcal{H}}_I$ in Eq. (B.2), the Eq. (C.2) becomes,

$$\begin{aligned}\frac{d}{dt}\langle\hat{\mathcal{N}}_\lambda\rangle = -\int_0^\infty d\tau\mathrm{Tr}_C\Big[&\left(\hat{\mathcal{S}}_\lambda^\dagger\hat{\mathcal{S}}_\lambda(-\tau)\hat{\rho}_C\right)C_\lambda(\tau) + \left(\hat{\rho}_C\hat{\mathcal{S}}_\lambda^\dagger(-\tau)\hat{\mathcal{S}}_\lambda\right)C_\lambda(-\tau)\\ &- \left(\hat{\mathcal{S}}_\lambda^\dagger(-\tau)\hat{\rho}_C\hat{\mathcal{S}}_\lambda\right)\tilde{C}_\lambda(\tau) - \left(\hat{\mathcal{S}}_\lambda^\dagger\hat{\rho}_C\hat{\mathcal{S}}_\lambda(-\tau)\right)\tilde{C}_\lambda(-\tau)\Big],\end{aligned} \tag{C.3}$$

where the correlations where defined in Eq. (B.10). Writting the conducting array part as Eq. (B.3) and the principal value theorem in Eq. (B.14), the Eq. (C.3) in secular approximation is,

$$\frac{d}{dt}\langle\hat{\mathcal{N}}_\lambda\rangle = -\sum_{n,m}\mathrm{Tr}_C\left[\frac{\kappa_\lambda^{(n,m)}}{2}\left(\hat{L}_{n,m}^\dagger\hat{L}_{n,m}\hat{\rho}_C + \hat{\rho}_C\hat{L}_{n,m}^\dagger\hat{L}_{n,m}\right) - \tilde{\kappa}_\lambda^{(n,m)}\hat{L}_{n,m}^\dagger\hat{\rho}_C\hat{L}_{n,m}\right], \tag{C.4}$$

where the effective transfer rates $\kappa_\lambda^{(n,m)}$ and $\tilde{\kappa}_\lambda^{(n,m)}$ are shown in Table B.2. Tracing over the conducting array degrees of freedom, the Eq. (C.4) becomes,

$$\frac{d}{dt}\langle\hat{\mathcal{N}}_\lambda\rangle = -\sum_{n,m}\left(\kappa_\lambda^{(n,m)}\rho_m - \tilde{\kappa}_\lambda^{(n,m)}\rho_n\right). \tag{C.5}$$